



Deposited via The University of Sheffield.

White Rose Research Online URL for this paper:

<https://eprints.whiterose.ac.uk/id/eprint/81768/>

Version: Accepted Version

Article:

Kesserwani, G. and Liang, Q. (2014) RKDG2 shallow-water solver on non-uniform grids with local time steps: Application to 1D and 2D hydrodynamics. *Applied Mathematical Modelling*, 39 (3-4). pp. 1317-1340. ISSN: 1872-8480

<https://doi.org/10.1016/j.apm.2014.08.009>

Reuse

Items deposited in White Rose Research Online are protected by copyright, with all rights reserved unless indicated otherwise. They may be downloaded and/or printed for private study, or other acts as permitted by national copyright laws. The publisher or other rights holders may allow further reproduction and re-use of the full text version. This is indicated by the licence information on the White Rose Research Online record for the item.

Takedown

If you consider content in White Rose Research Online to be in breach of UK law, please notify us by emailing eprints@whiterose.ac.uk including the URL of the record and the reason for the withdrawal request.

RKDG2 shallow-water solver on non-uniform grids with local time steps: application to 1D and 2D hydrodynamics

Georges Kesserwani ^a, Qiuhua Liang ^b

^a *Department of Civil and Structural Engineering, University of Sheffield, Mappin St., Sheffield S1 3JD, UK*

^b *School of Civil Engineering and Geosciences, Newcastle University, Newcastle upon Tyne NE1 7RU, UK*

Summary: This paper investigates Local Time Stepping (LTS) with the RKDG2 (second-order Runge-Kutta Discontinuous Galerkin) non-uniform solutions of the inhomogeneous SWEs (Shallow Water Equations) with source terms. A LTS algorithm – recently designed for homogenous hyperbolic PDE(s) – is herein reconsidered and improved in combination with the RKDG2 shallow-flow solver (LTS-RKDG2) including topography and friction source terms as well as wetting and drying. Two LTS-RKDG2 schemes that adapt 3 and 4 levels of LTSs are configured on 1D and/or 2D (quadrilateral) non-uniform meshes that, respectively, adopt 3 and 4 scales of spatial discretization. Selected shallow water benchmark tests are used to verify, assess and compare the LTS-RKDG2 schemes relative to their conventional Global Time Step RKDG2 alternatives (GTS-RKDG2) considering several issues of practical relevance to hydraulic modelling. Results show that the LTS-RKDG2 models could offer (depending on both the mesh setting and the features of the flow) comparable accuracy to the associated GTS-RKDG2 models with a savings in runtime of up to a factor of 2.5 in 1D simulations and 1.6 in 2D simulations.

Key-words: Shallow water equations; RKDG2 schemes; temporal adaptivity, non-uniform grids; conservative scheme; friction terms, computational efficiency, 1D and 2D hydraulic modelling.

*Corresponding author:

E-mails: g.kesserwani@sheffield.ac.uk; (G. Kesserwani) Qiuhua.Liang@ncl.ac.uk (Q. Liang)

26 **1. Introduction**

27 Explicit finite volume (FV) Godunov-type methods solving the shallow water equations
28 (SWEs) are relevant to simulate hydraulic problems because they excel in a distinctive
29 numerical formulation that incorporates widest range of spatial flow transients including
30 discontinuities [1, 2]. These models have received numerous developments [3, 4] and some
31 robust Godunov-type shallow water solvers have been successfully applied to support
32 practical applications [5, 6]. From an applied perspective, it is well-accepted that a *robust*
33 Godunov-type numerical solver should be able to maintain its stability and consistency when
34 a flow discontinuity develops, steep terrain gradients are present, a wet/dry front occurs, and
35 high roughness values are combined with very small water depths. In spite of all these
36 advances, it is still desirable to reduce the runtime of these explicit FV models. Parallelization
37 has alleviated this issue using extrinsic parallel computers [7, 8] as well as the intrinsic
38 shared-memory architecture of GPUs [9, 10]. However, the expanding power of parallelism
39 remains rather stagnant and is not without problems as such [11]. For example, the small
40 memory size of GPU computing cannot yet afford refined uniform-mesh simulations over
41 large spatial domain coverage. Thus, the size of the system in terms of the number of cells
42 remains a problem and, generally, to the interest of computational cost, allowing coarser cell
43 size in a form of a non-uniform mesh is certainly a benefit.

44 In this context, it is expected that the efficiency of an explicit numerical scheme may
45 suffer as the size of their time steps is restricted by the Courant-Friedrich-Lewy (CFL)
46 stability condition [12]. This criterion provides the maximum allowable Global Time Step
47 (GTS) permitted, which reduces proportional to a local increase in the velocity magnitude or
48 a local decrease in the cell size. Few refined cells may dictate a restrictive time step on the
49 whole non-uniform mesh, which may compromise by significantly longer runtimes.
50 Temporal adaptivity, or a local time step method (LTS), whereby the solutions on different

51 cell sizes are advanced by different time steps, may thus be beneficial to increase the
52 computational efficiency. In so doing, in the FV context, a local first-order Godunov-type
53 numerical formulation operating on a *small calculation stencil* appeared to be the most
54 accommodating setup to favour temporal data exchange between those heterogeneous cells of
55 the mesh [2]. However, first-order models are well-known to be diffusive – namely on coarse
56 portions of the mesh. Thus, the design of a higher-order accurate Godunov-type shallow water
57 model with a LTS algorithm could be beneficial and is the aim of this paper.

58 One convenient choice to do this is the use of a *local* spatial Discontinuous Galerkin
59 (DG) approximations paired with an explicit multi-stage Runge-Kutta (RK) time mechanism
60 (RKDG). RKDG schemes are reported to be convenient for (spatial) adaptive meshing
61 techniques and demonstrated to deliver converged solutions on coarse meshes better than
62 equally-accurate FV alternatives [13, 14]. An RKDG formulation can be regarded as an
63 extension to the original FV Godunov philosophy in the sense that inter-elemental flux
64 exchange evolves a finite series of local coefficients (spanning a polynomial solution) on
65 each mesh element; thus allows keeping the *calculation stencil small* despite the desired
66 order of accuracy. Practically speaking, the level of complexity, *robustness* and operational
67 efficiency of an RKDG formulation drastically increase with the desired formal accuracy-
68 order and the choice of the 2D mesh. A second-order accurate RKDG formulation (RKDG2)
69 is therefore sensible to deliver a shallow water model that handles flow simulations involving
70 topographic and friction effects, and flooding and drying processes [15-17]. Worth also
71 mentioning the work of Wirasaet et al. [18] that identified the suitability –in both accuracy
72 and efficiency– of quadrilateral meshes for low-order RKDG schemes over triangular
73 meshes.

74 Quite few published papers dealt with the design, implementation and verification of
75 LTS algorithms with Godunov-type shallow water solvers. Crossley and Wright [19] first

76 probed LTS algorithms in 1D hydrodynamic modelling using uniform meshes and based on
77 hypothetical test cases. Their findings revealed that LTS not only adds value in reducing
78 runtimes but also in augmenting the quality of the numerical solution. Later, Sanders [20]
79 explored a LTS method with a robust Godunov-type shallow water solver on 2D unstructured
80 triangular meshes and considering more challenging test cases, i.e. with frictional flow over
81 irregular topographies with wetting and drying. His conclusions reported a potential conflict
82 between the implicit friction term discretization (IFTD) –commonly used practice to stabilize
83 water flow simulations– and the LTS algorithm. Both of these investigations considered first-
84 order FV Godunov-type models recommended using a maximum level of four LTSs to avoid
85 introducing significant loss in accuracy or conservation relative to a conventional GTS
86 formulation. More recently, second-order accurate LTS methods have been integrated with
87 RKDG2 shallow water models following the multirate approach of Constantinescu and Sandu
88 [21]. Seny et al. [22] explored one LTS-RKDG2 approach on unstructured triangular meshes;
89 their approach considered flux monitoring to ensure conservation across interface cells but
90 was concluded to be not entirely stable and did not include source terms. Their findings also
91 point out that the multirate model is non-conservative for higher than second-order LTS-
92 RKDG formulation. Taran and Dawson [23] modified the multirate model to produce a
93 triangular mesh LTS-RKDG2 shallow water model that accommodates complex topography
94 domains and wetting and drying – albeit at introducing theoretical loss of accuracy. In both of
95 these papers, second-order mesh convergence was observed in ideal conditions (i.e.
96 frictionless and flat topography without wetting and drying) and speed up efficiency was
97 reported to be highly dependent on the mesh (with indications that it can accelerate efficiency
98 up to 2X).

99 In this work, a different LTS-RKDG2 shallow water solver is proposed and tested
100 with a particular focus on the applied aspects of hydraulic modelling and considering the case

101 of uniform but structured meshes in 1D and 2D (i.e. quadrilateral). The LTS algorithm of
102 Krivodonova [24] – particularly designed for RKDG2 schemes solving homogenous
103 conservation laws – is newly extended to the case of the (nonhomogeneous) SWEs, i.e. with
104 source terms and including wetting and drying [15, 17]. In Krivodonova [24], no information
105 was provided on the gain of efficiency owed to such an LTS-RKDG2 model and flux
106 conservation (in time) was enforced by a correction step adjusting the solution coefficients
107 (i.e. at large interface cells). Here, the extended LTS-RKDG2 algorithm is newly
108 reformulated so that: (i) it includes latest features relevant to applied hydraulic modelling
109 (e.g., local slope control [25], well-balanced property [26] and depth-positivity preserving
110 condition [27, 28]), (ii) flux conservation enforcement (in time) is dealt with by acting upon
111 the fluxes and (iii) new measures to minimize certain knock-on effects of the IFTD are
112 introduced. Another novel character of this paper is to systematically explore the ability of
113 the proposed LTS-RKDG2 shallow water solver relating to applied hydraulic modelling
114 including the issues of runtime efficiency and conservation on 1D vs. 2D mesh settings,
115 convergence of accuracy-order and towards a steady state, frictional flows and shock
116 capturing. In so doing, 1D and 2D implementations the proposed LTS-RKDG2 flow model
117 are verified and explored according to two different non-uniform meshes comprising
118 respectively three and four LTSs, and jointly with the conventional GTS-RKDG2
119 counterpart.

120 **2. Depth-averaged Shallow Water Equations (SWEs)**

121 From the principles of mass and momentum conservation, the mathematical model of SWEs
122 can be cast in a 2D conservative matrix form that involve as the main flow variables the free-
123 surface elevation (i.e. $\eta = h + z$) and the x -direction and y -direction components of unit-width
124 discharge, which are denoted, respectively, by hu and hv . Where h is the water depth, u and v

125 are, respectively, the velocity components in the x -direction and y -direction, and z the bed
 126 topography.

$$127 \quad \partial_t \mathbf{U} + \partial_x \mathbf{F}(\mathbf{U}) + \partial_y \mathbf{G}(\mathbf{U}) = \mathbf{S}(\mathbf{U}) \quad (1)$$

128 Where, (x, y) represent the Cartesian coordinates and t is the time. $\mathbf{U} = [\eta, hu, hv]^T$ is the
 129 vector of the conserved quantities or of flow variables, $\mathbf{F} = [hu, hu^2 + 0.5g(\eta^2 - 2\eta z), huv]^T$
 130 and $\mathbf{G} = [hv, huv, hv^2 + 0.5g(\eta^2 - 2\eta z)]^T$ are flux vectors relative to x - and y - directions, and
 131 \mathbf{S} is a vector containing the source terms. The source term vector \mathbf{S} can be further
 132 partitioned into $\mathbf{S} = \mathbf{S}_b + \mathbf{S}_f$ where $\mathbf{S}_b = [0, -g\eta \partial_x z, -g\eta \partial_y z]^T$ and $\mathbf{S}_f = [0, S_{fx}, S_{fy}]^T$,
 133 where $S_{fx} = -C_f u \sqrt{u^2 + v^2}$ and $S_{fy} = -C_f v \sqrt{u^2 + v^2}$, with $C_f = gn_M^2 / h^{1/3}$ (n_M is the
 134 Manning coefficient and g the constant gravitational acceleration).

135 In practical computation of flow hydrodynamics, the incorporation of the free-surface
 136 elevation variable η in the numerical discretization has proved useful to properly treat steep
 137 topographic slope (especially with the presence of a slope-limiter in the context of the
 138 RKDG2 framework [29]) and to implement a wetting and drying condition [30]. Therefore,
 139 recasting the SWEs so that [31] are the main the flow variables – whereas $\{h, u, v\}$ are the
 140 secondary variables obtained from the main variables – ensures better stability and
 141 convenience to integrate a wetting and drying condition [27].

142 **3. Non-uniform structured mesh**

143 Firstly, a problem domain is discretized using a coarse baseline mesh consisting of $M \times N$
 144 cells of size $\Delta x \times \Delta y$, which consists of coarsest cells, *i.e.* assigned a level of spatial
 145 refinement equal to ‘0’. Secondly, the baseline mesh is locally refined to enable higher level
 146 of spatial refinement varying from ‘1’ up to a maximum of ‘ lev_{max} ’ (where lev_{max} is a positive
 147 natural number). The refinement is performed in a fractal manner, *i.e.* the cell size reduces by

148 a factor of two whenever the refinement level increases ‘1’. Finally, the mesh is regularized
 149 so that it does not contain adjacent cells with sizes differing by more than a factor of two.

150 After these steps, a mesh embraces cells with different levels of refinement varying
 151 between ‘0’ and ‘ lev_{max} ’, where those with level ‘0’ are the largest and those with level
 152 ‘ lev_{max} ’ are the smallest. Thus a cell I_i with a level of refinement ‘ $lev(i)$ ’ ($0 \leq lev(i) \leq lev_{max}$)
 153 can be expressed as: $I_i = [x_{i-1/2}; x_{i+1/2}] \times [y_{i-1/2}; y_{i+1/2}]$, where $x_{i\pm 1/2} = x_i \pm \Delta x_i / 2$ and
 154 $y_{i\pm 1/2} = y_i \pm \Delta y_i / 2$, in which (x_i, y_i) represents the cell centre and $(\Delta x_i, \Delta y_i) = (\frac{\Delta x}{2^{lev(i)}}, \frac{\Delta y}{2^{lev(i)}})$ is
 155 its size, which is level-dependent.

156 4. Review of the Global Time Stepping RKDG2 scheme (GTS-RKDG2)

157 Over a cell ‘ I_i ’, the GTS-RKDG2 method solves for a *local planar* solution to (1), denoted by
 158 $\mathbf{U}_h = [\eta_h, (hu)_h, (hv)_h]^T$ that is engendered by three *local* coefficients, one cell-averaged data
 159 and two 1st-order-slope data (spanning the x - and y - directions). For consistency, these
 160 coefficients are denoted by $\mathbf{U}_i^0(t)$, $\mathbf{U}_i^{1x}(t)$ and $\mathbf{U}_i^{1y}(t)$, respectively [32, 33]. Using these
 161 coefficients, the local planar solution is expanded, i.e. $\mathbf{U}_h(x, y, t)|_{I_i} = \{\mathbf{U}_i^K(t)\}$ ($K = 0, 1x, 1y$),
 162 where it may be written as:

$$163 \quad \mathbf{U}_h(x, y, t)|_{I_i} = \mathbf{U}_i^0(t) + \mathbf{U}_i^{1x}(t) \left(\frac{x - x_i}{\Delta x_i / 2} \right) + \mathbf{U}_i^{1y}(t) \left(\frac{y - y_i}{\Delta y_i / 2} \right) \quad (\forall (x, y) \in I_i) \quad (2)$$

164 With given initial conditions, i.e. $\mathbf{U}_0(x, y) = \mathbf{U}(x, y, 0)$, the local expansion coefficients can be
 165 initialized (i.e. at $t = 0$ s) as

$$166 \quad \begin{aligned} \mathbf{U}_i^0(0) &= [\mathbf{U}_0(x_{i+1/2}, y_i) + \mathbf{U}_0(x_{i-1/2}, y_i) + \mathbf{U}_0(x_i, y_{i+1/2}) + \mathbf{U}_0(x_i, y_{i-1/2})] / 4 \\ \mathbf{U}_i^{1x}(0) &= [\mathbf{U}_0(x_{i+1/2}, y_i) - \mathbf{U}_0(x_{i-1/2}, y_i)] / 2 \\ \mathbf{U}_i^{1y}(0) &= [\mathbf{U}_0(x_i, y_{i+1/2}) - \mathbf{U}_0(x_i, y_{i-1/2})] / 2 \end{aligned} \quad (3)$$

167 The topography function must be similarly approximated (in space), within a local
 168 planar approximation, denoted here by $z_h(x, y)|_{I_i}$, to balance numerically flux gradients with

169 the topographic gradients (the *well-balanced* property) [26]. In the context of an RKDG2
 170 scheme, the local topography-associated expansion coefficients $\{z_i^K\}$ ($K = 0, 1x, 1y$) can be
 171 found in a similar way as described in (2) and (3) [29]. With this setting, the local bed slope
 172 gradient (within \mathbf{S}_b) writes $(\partial_x z_h(x, y)|_{I_i}, \partial_y z_h(x, y)|_{I_i}) = (2z_i^{1x} / \Delta x_i, 2z_i^{1y} / \Delta y_i)$.

173

174 4.1 Two-stage Runge-Kutta (RK) time stepping routine

175 On each local cell I_i , time evolution of the expansion coefficients, $\{\mathbf{U}_i^K(t)\}$, from ‘ t ’ to ‘ $t +$
 176 Δt_{GTS} ’ is performed by two-stage RK time stepping [34]. That is, denoting $\{\mathbf{U}_i^K\}^n$ and $\{\mathbf{U}_i^K$
 177 $\}^{n+1}$ the discrete coefficients at ‘ t ’, and ‘ $t + \Delta t_{GTS}$ ’ (respectively) local RK update write:

$$178 \quad \{\mathbf{U}_i^K\}^{n+1/2} = \{\mathbf{U}_i^K\}^n + \Delta t_{GTS} \{\mathbf{L}_i^K\}^n \quad (4)$$

$$179 \quad \{\mathbf{U}_i^K\}^{n+1} = \frac{1}{2} \left[\{\mathbf{U}_i^K\}^n + \{\mathbf{U}_i^K\}^{n+1/2} + \Delta t_{GTS} \{\mathbf{L}_i^K\}^{n+1/2} \right] \quad (5)$$

180 To ease technical presentation (coming next), the RK stages in (4) and (5), respectively, are
 181 hereafter referred to RK1 and RK2, which are recalled below:

- 182 • RK1 uses the coefficients $\{\mathbf{U}_i^K\}^n$ (at time ‘ t ’) to produce coefficients, $\{\mathbf{U}_i^K\}^{n+1/2}$, after
 183 halfway step of time (at ‘ $t^* = t + \Delta t_{GTS} / 2$ ’).
- 184 • RK2 further uses the coefficients of $\{\mathbf{U}_i^K\}^{n+1/2}$ to produce coefficients, $\{\mathbf{U}_i^K\}^{n+1}$, after
 185 one time step (at ‘ $t + \Delta t_{GTS}$ ’).

186 In (4) and (5), $\{\mathbf{L}_i^K\}$ are locally-conservative **DG2** (Discontinuous Galerkin 2nd-order) spatial
 187 operators (details in Subsection 4.2) that are evaluated from the expansion coefficients;
 188 whereas Δt_{GTS} denotes the Global Time Step (GTS) that is restricted by the Courant-
 189 Friedrichs-Lewy condition (CFL) stability condition with a CFL number equal to 0.3 [33]. In

190 this work, Δt_{GTS} is evaluated according to the coefficients of the cell-averaged data as
 191 described Eq. (6) below:

$$192 \quad \Delta t_{GTS} = \text{CFL} \times \min_i \left(\frac{\Delta x_i}{\left| (u_i^0)^n \right| + \sqrt{g(h_i^0)^n}}, \frac{\Delta y_i}{\left| (v_i^0)^n \right| + \sqrt{g(h_i^0)^n}} \right) \quad (6)$$

193 Obviously, from (6), on a non-uniform mesh, Δt_{GTS} is governed by the smallest cells (*i.e.*
 194 those with the highest refinement level) and tends to decrease when more depth in refinement
 195 level is allowed ($\Delta t \rightarrow 0$ when $lev_{max} \rightarrow \infty$).

196

197 4.2 Local DG2 space operators

198 After application of the finite element weak formulation, to (1), and the particular adoption of
 199 Legendre basis as *local* basis functions [32, 33], a decoupled set of ODEs is obtained for the
 200 spatial update of the time-derivative of each local coefficients, namely:

$$201 \quad \left\{ \partial_t \mathbf{U}_i^K(t) \right\} = \left\{ \mathbf{L}_i^K \right\} \quad (K = 0, 1x, 1y) \quad (7)$$

202 where, $\left\{ \mathbf{L}_i^K \right\}$ are nonlinear vectors of space-functions representing the flux derivatives and
 203 the source terms in (1), which can be manipulated to:

$$204 \quad \mathbf{L}_i^0 = -\frac{1}{\Delta x_i} \left(\tilde{\mathbf{F}}_i^E - \tilde{\mathbf{F}}_i^W \right) - \frac{1}{\Delta y_i} \left(\tilde{\mathbf{G}}_i^N - \tilde{\mathbf{G}}_i^S \right) + \mathbf{S} \left(\mathbf{U}_i^0, z_i^{1x}, z_i^{1y} \right) \quad (8)$$

$$205 \quad \mathbf{L}_i^{1x} = -\frac{3}{\Delta x_i} \left\{ \tilde{\mathbf{F}}_i^E + \tilde{\mathbf{F}}_i^W - \mathbf{F} \left(\mathbf{U}_i^0 + \frac{\hat{u}_i^{1x}}{\sqrt{3}}, z_i^0 + \frac{z_i^{1x}}{\sqrt{3}} \right) - \mathbf{F} \left(\mathbf{U}_i^0 - \frac{\hat{u}_i^{1x}}{\sqrt{3}}, z_i^0 - \frac{z_i^{1x}}{\sqrt{3}} \right) \right. \\ \left. - \frac{\Delta x_i \sqrt{3}}{6} \left[\mathbf{S} \left(\mathbf{U}_i^0 + \frac{\hat{u}_i^{1x}}{\sqrt{3}}, z_i^{1x} \right) - \mathbf{S} \left(\mathbf{U}_i^0 - \frac{\hat{u}_i^{1x}}{\sqrt{3}}, z_i^{1x} \right) \right] \right\} \quad (9)$$

$$206 \quad \mathbf{L}_i^{1y} = -\frac{3}{\Delta y_i} \left\{ \tilde{\mathbf{G}}_i^N + \tilde{\mathbf{G}}_i^S - \mathbf{G} \left(\mathbf{U}_i^0 + \frac{\hat{u}_i^{1y}}{\sqrt{3}}, z_i^0 + \frac{z_i^{1y}}{\sqrt{3}} \right) - \mathbf{G} \left(\mathbf{U}_i^0 - \frac{\hat{u}_i^{1y}}{\sqrt{3}}, z_i^0 - \frac{z_i^{1y}}{\sqrt{3}} \right) \right. \\ \left. - \frac{\Delta y_i \sqrt{3}}{6} \left[\mathbf{S} \left(\mathbf{U}_i^0 + \frac{\hat{u}_i^{1y}}{\sqrt{3}}, z_i^{1y} \right) - \mathbf{S} \left(\mathbf{U}_i^0 - \frac{\hat{u}_i^{1y}}{\sqrt{3}}, z_i^{1y} \right) \right] \right\} \quad (10)$$

207 When evaluating the **DG2** operators (8)-(10), a number of essential (spatial)
208 treatments must be considered to maintain stability and robustness for realistic flow
209 modelling applications. These treatments are summarized here (to save space) as their details
210 can be found in Kesserwani and Liang [17]. First, local slope coefficients (i.e. \mathbf{U}_i^{1x} and \mathbf{U}_i^{1y})
211 that could cause numerical instability at sharp solution's gradient are identified and limited
212 [25]; after slope coefficients control, they are appended with a “hat” (i.e. $\hat{\mathbf{U}}_i^{1x}$ and $\hat{\mathbf{U}}_i^{1y}$).
213 Second, the discontinuous nature of the local approximate solution \mathbf{U}^h , at the faces separating
214 two adjacent cells, is incorporated via the HLLC approximate Riemann solver. The HLLC
215 evaluations recall information from direct neighbour cells to then produce the numerical flux
216 estimates $\tilde{\mathbf{F}}_i^E$, $\tilde{\mathbf{F}}_i^W$, $\tilde{\mathbf{G}}_i^N$ and $\tilde{\mathbf{G}}_i^S$ at, respectively, the eastern, western, northern and southern
217 faces of each cell I_i [2]. Third, conservative spatial flux computation of these fluxes needed to
218 ensured when cell I_i shares an edge (or more) with two finer cells (on a 2D mesh) [17]. Last,
219 it is important to ensure the positivity of the flow variables with time evolution, which is here
220 done based on the wetting and drying condition described in [35] (applied to revise the
221 coefficients prior to evaluating any of the components in Eqs. (8)-(10)).

222

223 **4.3 Implicit Friction Term Discretization (IFTD)**

224 When modelling water flow over dry zone with high roughness, the water depth close to the
225 wet/dry front can be very small and may lead to numerical instabilities if the friction source
226 term \mathbf{S}_f is explicitly discretized, within (8)-(10) [36]. Separate implicit discretization is
227 largely recommended for handling the friction terms in order to avoid numerical instabilities.
228 By denoting the local approximate friction term by $(\mathbf{S}_f)_h$, the update due to the friction term
229 is done by the following splitting implicit scheme:

$$230 \quad \partial_t \mathbf{U}_h = (\mathbf{S}_f)_h^{n+1} \quad (11)$$

231 Since the friction increment is zero for the continuity equation, only the momentum
 232 components are actually considered, i.e.

$$233 \quad \partial_t(hu)_h = (S_{fx})_h^{n+1} \quad (12)$$

$$234 \quad \partial_t(hv)_h = (S_{fy})_h^{n+1} \quad (13)$$

235 Eqs (12) and (13) may be respectively approximated by

$$236 \quad \frac{(hu)_h^{n+1} - (hu)_h^n}{\Delta t_{GTS}} = (S_{fx})_h^n + \frac{\partial(S_{fx})_h^n}{\partial(hu)} \left[(hu)_h^{n+1} - (hu)_h^n \right] \quad (14)$$

$$237 \quad \frac{(hv)_h^{n+1} - (hv)_h^n}{\Delta t_{GTS}} = (S_{fy})_h^n + \frac{\partial(S_{fy})_h^n}{\partial(hv)} \left[(hv)_h^{n+1} - (hv)_h^n \right] \quad (15)$$

238 From Eqs (14) and (15), the friction update formulae for the discharges components $(hu)_h$ and
 239 $(hv)_h$ may be produced

$$240 \quad (hu)_h^{n+1} = (hu)_h^n + \Delta t_{GTS} \frac{(S_{fx})_h^n}{(Du)_h^n} \quad (16)$$

$$241 \quad (hv)_h^{n+1} = (hv)_h^n + \Delta t_{GTS} \frac{(S_{fy})_h^n}{(Dv)_h^n} \quad (17)$$

242 in which Du and Dv are implicit coefficients that respectively given by

$$243 \quad (Du)_h^n = 1 + \Delta t_{GTS} \left(\frac{C_f}{h} \frac{2u^2 + v^2}{\sqrt{u^2 + v^2}} \right)_h^n \quad (18)$$

$$244 \quad (Dv)_h^n = 1 + \Delta t_{GTS} \left(\frac{C_f}{h} \frac{u^2 + 2v^2}{\sqrt{u^2 + v^2}} \right)_h^n \quad (19)$$

245 This IFTD automatically ensures $(hu)_h^{n+1} \times (hu)_h^n \geq 0$ and $(hv)_h^{n+1} \times (hv)_h^n \geq 0$, and will not
 246 predict reversed flow. In the current GTS-RKDG2 model, the splitting implicit scheme (16)
 247 and (17) are applied to each wet cell I_i to add the contribution of friction into the average

248 coefficients $(hu)_i^0$ and $(hv)_i^0$, respectively, in a pointwise manner, prior to the RK1 stage and
 249 the RK2 stage. In order to add the friction contribution to the slope coefficients, i.e. $(hu)_i^K$
 250 and $(hv)_i^K$ ($K \neq 0$), one simple way is to first perform a pointwise friction update at
 251 corresponding local Gaussian points and then deduce the slopes coefficients by a local *planar*
 252 P^1 -projection [29, 33]. For instance, the friction increment within the slope coefficients
 253 $(hu)_i^K$, ($K \neq 0$), can be added as follows

$$254 \quad (hu)_i^{1x} = \frac{\sqrt{3}}{2} \left[(hu)_{G1}^{n+1} - (hu)_{G2}^{n+1} \right] \quad (20)$$

$$255 \quad (hu)_i^{1y} = \frac{\sqrt{3}}{2} \left[(hu)_{P1}^{n+1} - (hu)_{P2}^{n+1} \right] \quad (21)$$

256 $(hu)_{G1,G2}^{n+1}$ and $(hu)_{P1,P2}^{n+1}$ are pointwise output of the friction update (16) evaluated for
 257 $(hu)_{G1,G2}^n = \left[(hu)_i^0 \pm (hu)_i^{1x} / \sqrt{3} \right]^n$ and $(hu)_{P1,P2}^n = \left[(hu)_i^0 \pm (hu)_i^{1y} / \sqrt{3} \right]^n$, respectively. By
 258 analogy, the friction contribution can be added to $(hv)_i^K$, ($K \neq 0$).

259 Despite ensuring stability, the IFTD may lead to a loss in the discrete balance among
 260 fluxes and topographic source terms (i.e. *well-balanced* property [26, 28]), particularly when
 261 modelling steady flow problems over uneven topographies with non-zero velocities (refer to
 262 the detailed analysis in [37]). Furthermore, the IFTD relationships (16) and (17), which does
 263 not pose a problem with the GTS-RKDG2 scheme, may conflict with a LTS scheme (will be
 264 discussed in Subsection 5.3.1 and illustrated in Subsection 6.1).

265

266 4.4 Reduced 1D GTS-RKDG2 formulation

267 Neglecting the y -direction components, the vector \mathbf{G} vanishes in (1) and the system reduces
 268 to two equations with two unknowns; now $\mathbf{U} = [\eta, hu]^T$, $\mathbf{F} = [hu, hu^2 + 0.5g(\eta^2 - 2\eta z)]^T$,

269 $\mathbf{s}_b = [0, -g\eta \partial_x z]^T$ and $\mathbf{S}_f = [0, S_{fx}]^T$. The 1D version of the GTS-RKDG2 scheme uses
 270 local *linear* solutions and topography approximations engendered by two coefficients (one
 271 cell-averaged and one for the monodirectional slope), i.e. $\{\mathbf{U}_i^K(t)\}$ and $\{z_i^K\}$ ($K = 0, 1x$).
 272 That is, over a 1D local cell $I_i = [x_{i-1/2}, x_{i+1/2}]$ the flow solution (and similarly the topography
 273 apart from being static-in-time) expands as:

$$274 \quad \mathbf{U}_h(x, t)|_{I_i} = \mathbf{U}_i^0(t) + \mathbf{U}_i^{1x}(t) \left(\frac{x - x_i}{\Delta x_i / 2} \right) \quad (22)$$

275 The **DG2** spatial derivative operators reduce to two

$$276 \quad \begin{aligned} \mathbf{L}_i^0 &= -\frac{1}{\Delta x_i} (\tilde{\mathbf{F}}_i^E - \tilde{\mathbf{F}}_i^W) + \mathbf{S}(\mathbf{U}_i^0, z_i^1) \\ \mathbf{L}_i^{1x} &= -\frac{3}{\Delta x_i} \left\{ \tilde{\mathbf{F}}_i^E + \tilde{\mathbf{F}}_i^W - \mathbf{F}\left(\mathbf{U}_i^0 + \frac{\hat{U}_i^{1x}}{\sqrt{3}}, z_i^0 + \frac{z_i^{1x}}{\sqrt{3}}\right) - \mathbf{F}\left(\mathbf{U}_i^0 - \frac{\hat{U}_i^{1x}}{\sqrt{3}}, z_i^0 - \frac{z_i^{1x}}{\sqrt{3}}\right) \right. \\ &\quad \left. - \frac{\Delta x_i \sqrt{3}}{6} \left[\mathbf{S}\left(\mathbf{U}_i^0 + \frac{\hat{U}_i^{1x}}{\sqrt{3}}, z_i^1\right) - \mathbf{S}\left(\mathbf{U}_i^0 - \frac{\hat{U}_i^{1x}}{\sqrt{3}}, z_i^1\right) \right] \right\} \end{aligned} \quad (23)$$

277 The RK1 and RK2 stages (4) and (5), together with the IFTD, apply straightforwardly to
 278 locally advance coefficients $\{\mathbf{U}_i^K(t)\}$ in time [35]. It is worth commenting that, relative to the
 279 2D GTS-RKDG2 model, its 1D version is expected to be more efficient in that: first, it
 280 involves twice less inter-cell flux calculations; second, it needs twice less the number of
 281 operations to achieve the RK updates and has four times less operations in each call to the
 282 IFTD. Above all, the 1D version is not subjected to (extrinsic) inter-scales flux conservation
 283 reinforcement (in space) at heterogeneous cells [17]; thus could be also more conservative.

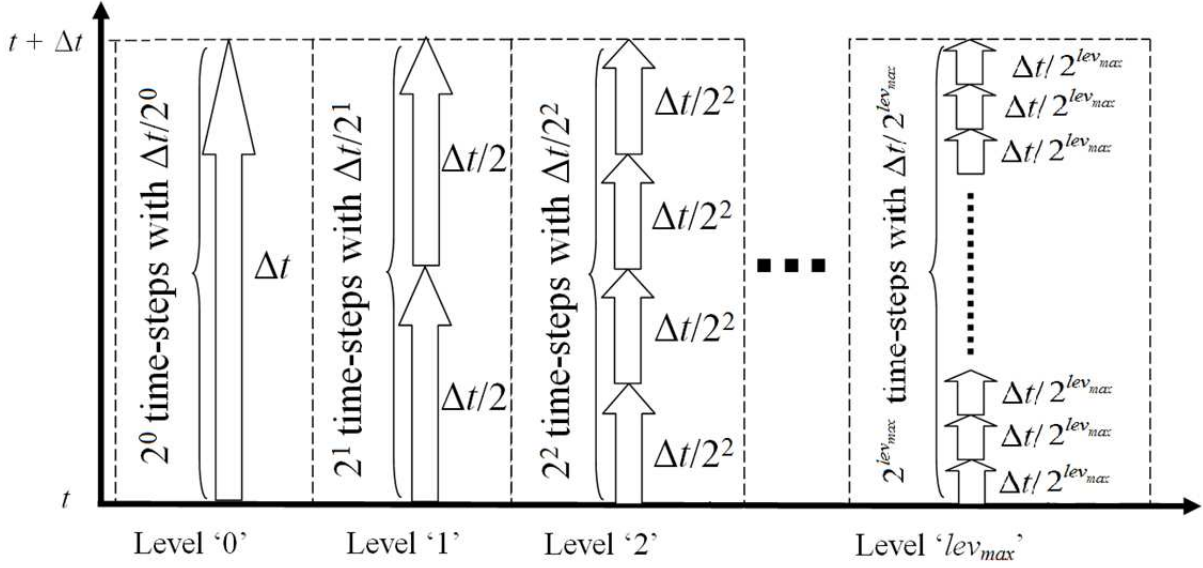


Fig. 1: LTS-RKDG2 calculation(s) to the coefficients from ' t ' to ' $t + \Delta t$ ' on a mesh with levels of refinement ' 0 ', ..., ' lev_{max} ', where a '**thick arrow**' = one LTS-RKDG2 calculation. The LTS-RKDG2 update is first achieved at cells with the level ' 0 '. Then, the calculation moves to those cells with level ' 1 ', and so on until those cells with the highest level ' lev_{max} ' are reached after $2^{lev_{max}}$ LTS-RKDG2 calculations.

284

285 5. New Local-Time-Stepping RKDG2 flow model (LTS-RKDG2)

286 In this section, the second-order LTS approach of Krivodonova [24] is integrated with the
 287 RKDG2 model [15] to form the so-called LTS-RKDG2 formulation. Their combination is
 288 here redesigned in order to accommodate the applied features of shallow flow simulations.
 289 For convenience of presentation, the LTS-RKGD2 method is described for the 1D version (as
 290 the description of the 2D version reads by analogy).

291

292 5.1 Basic concept

293 Assuming (for simplicity) that the maximum wave speed does not significantly influence the
 294 local CFL number, the LTS (Local Time Step) relative to cell I_i is solely dependent on its
 295 level of refinement $lev(i)$, or cell size $\Delta x_i = \Delta x/2^{lev(i)}$. Here, Δt denotes the maximum time step
 296 allowed that is yet relative to the coarsest resolution (cells with level ' 0 ' of refinement), i.e.

297

$$\Delta t = \Delta t_{GTS} \times 2^{lev_{max}} \quad (24)$$

298 As illustrates in Fig. 1, LTS-RKDG2 calculation(s) are locally performed with the
 299 LTS Δt , $\Delta t/2$, $\Delta t/2^2$, ..., $\Delta t/2^{lev_{max}}$, orderly, on the cells with level '0', '1', '2', ..., ' lev_{max} ' to
 300 progressively advance their coefficients 2^0 LTS, 2^1 LTSs, 2^2 LTSs, ..., $2^{lev_{max}}$ LTSs,
 301 respectively. At the first iteration, the LTS-RKDG2 calculation operates at cells with level '0'
 302 to directly lift their coefficients to time ' $t + \Delta t$ ' (i.e. in one round). At the second iteration,
 303 LTS-RKDG2 calculations are undertaken at cells with level '1' (i.e. in two rounds), and so
 304 on, until the finest cells with level ' lev_{max} ' are fully updated after $2^{lev_{max}}$ rounds. Therefore,
 305 cells are crossed according to their level of refinement on a mesh that comprises "*inner cells*"
 306 and "*interface cells*". When cell I_i has all of its neighbours of equal size, it will be an *inner*
 307 *cell*; otherwise, if at least one of its neighbours has different size, cell I_i will be an *interface*
 308 *cell* (so will the neighbour be). When I_i is an *inner cell*, LTS-RKDG2 calculation(s) are
 309 straightforward and actually stem from a series of GTS-RKDG2 calculation(s) using the LTS
 310 time step $\Delta t/2^{lev(i)}$ (instead of Δt_{GTS}) across $2^{lev(i)}$ rounds.

311 However, when I_i is an *interface cell* at least one of its adjacent neighbours has a
 312 different refinement level. In what follows, to ease the details, we assume the eastern
 313 neighbour cell I_{in} is such a neighbour, which is also an *interface cell*. In this scenario, the
 314 LTS-RKDG2 calculation at *interface cells* $\{I_i, I_{in}\}$ faces different temporal resolutions on
 315 cells I_i and I_{in} . To accommodate this difference, synchronized '*ghost*' coefficients must be
 316 produced to complete the LTS-RKDG2 calculation(s) across first the inner RK1 and RK2
 317 stages, and then the LTSs (as described in Section 5.2).

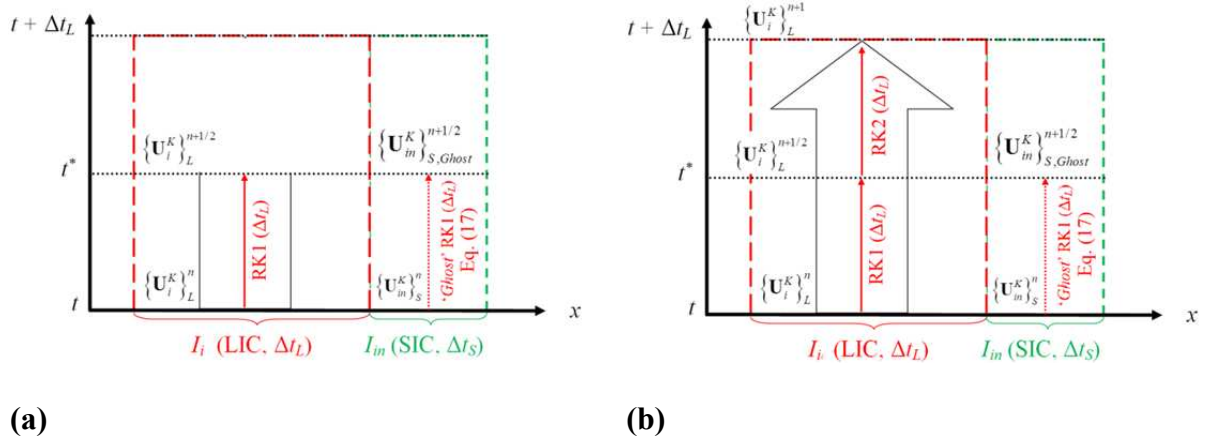


Fig. 2. LTS-RKDG2 calculation at the LIC I_i (neighbourred by a SIC I_{in}) to advance its coefficients from time ‘ t ’ to time ‘ $t + \Delta t_L$ ’, where a ‘*thin arrow*’ = one RK stage, ‘*thick arrow*’ = one-time-step, ‘*straight line*’ = ‘*actual*’ advancement and ‘*dashed line*’ = ‘*ghost*’ advancement.

318

319 5.2 LTS-RKDG2 calculation(s) at the interface cells $\{I_i, I_{in}\}$

320 Since the mesh is regularized (see Section 3) and the calculation is recursive, it suffices to
 321 explain the LTS-RKDG2 calculation(s) when cells I_i and I_{in} are one refinement level
 322 different. Without loss of generality, assume cells I_i and I_{in} have, respectively, ‘0’ and ‘1’ as a
 323 refinement levels. Cells I_i and I_{in} can, respectively, be viewed as “*Large Interface Cell*” (LIC)
 324 and “*Small Interface Cell*” (SIC); consistently, their associated LTS, coefficients and fluxes
 325 will be appended with the subscripts ‘ L ’ and ‘ S ’, respectively. Firstly, *one* LTS-RKDG2
 326 calculation is applied to update the ‘*actual*’ coefficients at the LIC (I_i) while employing
 327 ‘*ghost*’ synchronized coefficients from the SIC (I_{in}) [Subsection 5.2.1]. Next, *two* LTS-
 328 RKDG2 calculations are applied to update the ‘*actual*’ coefficients are at the SIC (I_{in}) while
 329 using ‘*ghost*’ coefficients from the LIC (I_i) [Subsection 5.2.2].

330

331 5.2.1 Coefficients update at the LIC (I_i)

332 At the LIC I_i , LTS-RKDG2 calculation starts from the coefficients at time ‘ t ’, i.e. $\{\mathbf{U}_i^K\}_L^n$,
 333 with the LTS $\Delta t_L = \Delta t/2^0$. At ‘ t ’, the coefficients at the SIC I_{in} , i.e. $\{\mathbf{U}_{in}^K\}_S^n$, are also available.

334 **DG2** space operators on I_i , i.e. $\{\mathbf{L}_i^K\}_L^n$, can be obtained leading to (after RK1) the ‘*actual*’
 335 coefficients on I_i at ‘ $t^* = t + \Delta t_L/2$ ’, i.e. $\{\mathbf{U}_i^K\}_L^{n+1/2}$, (Fig. 2a — ‘straight thin arrow’ in the
 336 left-hand-side). Equally, RK1 is applied on I_{in} but with the LTS Δt_L leading to time-
 337 matching ‘*ghost*’ coefficients, i.e. $\{\mathbf{U}_{in}^K\}_{S,Ghost}^{n+1/2}$ (Fig. 2a — ‘dashed thin arrow’ in the right-
 338 hand-side), namely:

$$339 \quad \{\mathbf{U}_{in}^K\}_{S,Ghost}^{n+1/2} = \{\mathbf{U}_{in}^K\}_S^n + \Delta t_L \{\mathbf{L}_{in}^K\}_S^n \quad (25)$$

340 Again, **DG2** space operators on I_i , i.e. $\{\mathbf{L}_i^K\}_L^{n+1/2}$, can be now obtained for evaluation in RK2
 341 advancing thereby to produce the ‘*actual*’ coefficients to time ‘ $t + \Delta t_L$ ’, i.e. $\{\mathbf{U}_i^K\}_L^{n+1}$ (Fig. 2b
 342 — second ‘straight thin arrow’ and the ‘thick arrow’ in the left-hand-side).

343

344 5.2.2 Coefficients update at the SIC (I_{in})

345 Calculation restarts (time ‘ t ’) at the SIC I_{in} with the LTS $\Delta t_S = \Delta t_L/2$; thus two LTS-RKDG2
 346 calculations are needed to move its ‘*actual*’ coefficients to ‘ $t + \Delta t_L$ ’ (i.e. across two rounds).
 347 Before detailing these calculations, it should be noted that any past ‘*ghost*’ information on I_{in}
 348 must be ignored; whereas some past ‘*actual*’ information on I_i are needed (i.e. the DG2 space
 349 operator records across inner time stages) to define the following quadratic function:

$$350 \quad \{\phi_i^K(\tau)\} = \{\mathbf{U}_i^K\}_L^n + \{\mathbf{L}_i^K\}_L^n (\tau - t) + \frac{\{\mathbf{L}_i^K\}_L^{n+1/2} - \{\mathbf{L}_i^K\}_L^n}{2\Delta t_L} (\tau - t)^2 \quad (26)$$

351 that is needed to interpolate ‘*ghost*’ coefficients on I_i at a fractional time-step $\tau \in [t; t + \Delta t_L[$

352 and an associated intermediate time-stage at $\tau^* \in [\tau; t + \Delta t_L[$, i.e.

$$353 \quad \{\mathbf{U}_i^K(\tau)\}_{L,Ghost}^n = \{\phi_i^K(\tau)\} \quad (27)$$

$$354 \quad \{\mathbf{U}_i^K(\tau^*)\}_{L,Ghost}^{n+1/2} = \{\mathbf{U}_i^K(\tau)\}_{L,Ghost}^n + \Delta t_S \frac{d}{d\tau} \{\phi_i^K(\tau)\} \quad (28)$$

355 • In the first LTS-RKDG2 calculation, coefficients over I_{in} are advanced one LTS to ' $t_2 = t$
356 + Δt_S '. Calculation starts from the coefficients available at ' t ', i.e. $\{\mathbf{U}_{in}^K\}_S^n$ and $\{\mathbf{U}_i^K\}_L^n$,
357 that give the **DG2** operators on I_{in} , i.e. $\{\mathbf{L}_{in}^K\}_S^n$, which in turn (via RK1) yield the '*actual*'
358 coefficients at ' $t_1^* = t + \Delta t_S/2$ ', i.e. $\{\mathbf{U}_{in}^K\}_S^{n+1/2}$ (Fig. 3a — 'straight thin arrow' at the
359 right-hand-side). Meanwhile, on I_i , synchronized '*ghost*' coefficients, i.e. $\{\mathbf{U}_i^K\}_{L,Ghost}^{n+1/2}$, are
360 reconstructed (Fig. 3a — 'dashed thin arrow' at the left-hand-side) by [(27) and (28)
361 evaluated at $\tau = t_1^*$]:

$$\{\mathbf{U}_i^K\}_{L,Ghost}^{n+1/2} = \{\mathbf{U}_i^K\}_L^n + \Delta t_S \{\mathbf{L}_i^K\}_L^n \quad (29)$$

362 Local **DG2** space operators $\{\mathbf{L}_{in}^K\}_S^{n+1/2}$ on I_{in} can be now evaluated to (via RK2) yield the
363 '*actual*' coefficients at ' t_2 ', i.e. $\{\mathbf{U}_{in}^K\}_S^{n+1}$ (Fig. 3c — second 'straight thin arrow' and the
364 'thick arrow' at the right-hand-side). Meanwhile, again, synchronized (at ' t_2 ') '*ghost*'
365 coefficients, on I_i , i.e. $\{\mathbf{U}_i^K\}_{L,Ghost}^{n+1}$, are reconstructed (Fig. 3b — second 'dashed thin
366 arrow' and the overall 'thick dashed arrow' at the left-hand-side) [via (26) and (27)
367 evaluated at $\tau = t_2$] by:

$$\{\mathbf{U}_i^K\}_{L,Ghost}^{n+1} = \{\phi_i^K(t_2)\} = \{\mathbf{U}_i^K\}_L^n + \Delta t_S \{\mathbf{L}_i^K\}_L^n + (\Delta t_S)^2 \frac{\{\mathbf{L}_i^K\}_L^{n+1/2} - \{\mathbf{L}_i^K\}_L^n}{2\Delta t_L} \quad (30)$$

370 • Prior to the second LTS-RKDG2 calculation, both '*actual*' and '*ghost*' coefficients (at I_{in}
371 and I_i) are reinitialized at ' t_2 ' (see Fig. 3d): $\{\mathbf{U}_{in}^K\}_S^n \leftarrow \{\mathbf{U}_{in}^K\}_S^{n+1}$ & $\{\mathbf{U}_i^K\}_L^n \leftarrow \{\mathbf{U}_i^K\}_{L,Ghost}^{n+1}$
372 (all variable relevant to intermediate time-stage $\{\cdot\}^{n+1/2}$ can be now reused). Calculation
373 starts from the initial coefficients at ' t_2 ', i.e. $\{\mathbf{U}_{in}^K\}_S^n$ and $\{\mathbf{U}_i^K\}_L^n$, leading to (after
374 calculation of $\{\mathbf{L}_{in}^K\}_S^n$ on I_{in} and then via and RK1) the '*actual*' coefficients at ' $t_2^* = t_2 +$
375 $\Delta t_S/2$ ', i.e. $\{\mathbf{U}_{in}^K\}_S^{n+1/2}$ (Fig. 3e—right part along the third 'straight thin arrow').

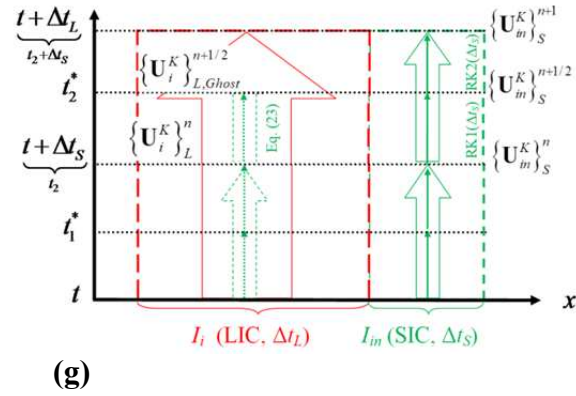


Fig. 3. LTS-RKDG2 calculation at the SIC I_i (neighboured by the LIC I_{in}) to advance its coefficients from time ' t ' to time ' $t + \Delta t_L$ ' in two consecutive rounds. A **'thin arrow'** = one-time-stage, **'thick arrow'** = one-time-step, **'straight line'** = *'actual'* advancement and **'dashed line'** = *'ghost'* advancement.

382

383 5.3 Specific issues relevant to applied hydraulic modelling

384 During the LTS-RKDG2 calculation(s), slope-limiting and wetting and drying do not appear
 385 to pose any specific technical problems. In contrast, more computational work is found
 386 necessary to properly handle the IFTD (Subsection 5.3.1) and conserve the fluxes in time
 387 (Subsection 5.3.2) at *interface cells*.

388

389 5.3.1 Hybrid explicit-implicit discretization of the friction term

390 When using the implicit friction source term discretization (IFTD) [see Subsection 4.3]
 391 across the LTS-RKDG2 calculations, its aforementioned side effect of disturbing the *well-*
 392 *balanced* property may magnify at *inner cells* proportional to an increase in the refinement
 393 level (see also numerical experiments in Subsection 6.1). On the other hand, the different
 394 LTSs within the IFTD complicate its integration during the LTS-RKDG2 calculations at
 395 *interface cells* (i.e. to avoid duplicate use of the IFTD at the same *interface cell* with two
 396 different LTSs). This complication stems from the need to produce extra phases of *'ghost'*
 397 friction advancement, and removal, in line with the *'ghost'* coefficients advancement
 398 (outlined before in Subsections 5.2.1 and Subsection 5.2.2).

399 One convenient way to avoid this complication is to restrict the usability of the IFTD
400 to those cells where the water height may potentially become infinitesimal; whereas
401 elsewhere (at wet cells) use explicit friction source term discretization in the **DG2** operators
402 (23) [free from any time-step dependence]. In this work, the IFTD is only applied locally at a
403 cell I_i when a small water level occurs in the calculation stencil containing cell I_i and its direct
404 neighbours, e.g. in the 1D when:

$$405 \quad \min(h_{i-1}^0, h_i^0, h_{i+1}^0) \leq 3\% \times h^{\max}(t) \quad (32)$$

406 where $h^{\max}(t)$ represents the maximum water level spanning the wet domain at time ‘ t ’. The
407 3% is a user-selected threshold, which means that the IFTD will be active at, or around, those
408 cell where the RKDG2 calculation involves, at least, a depth that is smaller than 3% of the
409 maximum depth.

410 Now the IFTD implementation with LTS-RKDG2 calculation(s) is described, which
411 could occur at either *inner cells* or *interface cells*. At *inner cells* the IFTD applies
412 (recursively) a similar way as with the GTS-RKDG2 scheme. In contrast, at *interface cells*
413 the IFTD needs a careful treatment across RK1 and RK2 stages where ‘Ghost’ data change
414 for the different LTSs (Subsections 5.2.1 and 5.2.2). Here, we detail the application of the
415 IFTD within the LTS-RKDG2 calculation(s) consistent with *interface cell* $\{I_i, I_{in}\}$.

- 416 • During the LTS-RKDG2 calculation at the LIC, the IFTD step (16) applies at I_i (resp. at
417 I_{in}) to amend the ‘*actual*’ (resp. ‘*ghost*’) discharge coefficients within $\{\mathbf{U}_i^K\}_L^n$ and $\{\mathbf{U}_{in}^K\}$
418 $_S^n$. Then, once coefficients $\{\mathbf{U}_i^K\}_L^{n+1/2}$ and $\{\mathbf{U}_{in}^K\}_{S,Ghost}^{n+1/2}$ are in place (Subsection 5.2.1), the
419 IFTD step (16) is again applied at I_i (resp. at I_{in}) to amend their ‘*actual*’ (resp. ‘*ghost*’) discharge
420 coefficients. However, once ‘*actual*’ coefficients at I_i are lifted to ‘ $t + \Delta t_L$ ’, it is
421 necessary to restore their initial (*frictionless* discharge) relative to time ‘ t ’.

- 422 • During the LTS-calculations at the SIC I_{in} , no further treatment is here needed. In effect,

423 after the LTS-RKDG2 calculation at the LIS I_i : (a) its initial discharge coefficients in $\{$

424 $\mathbf{U}_i^K\}_L^n$ have been reset to frictionless; (b) the (saved) **DG2** operators $\{\mathbf{L}_i^K\}_L^n$ and $\{\mathbf{L}_i^K\}$

425 $^{n+1/2}_L$ already include the ‘actual’ effects due to friction. Thus, ‘ghost’ coefficients at I_i ,

426 reconstructed by (29)-(31), are expected to include the contribution of friction.

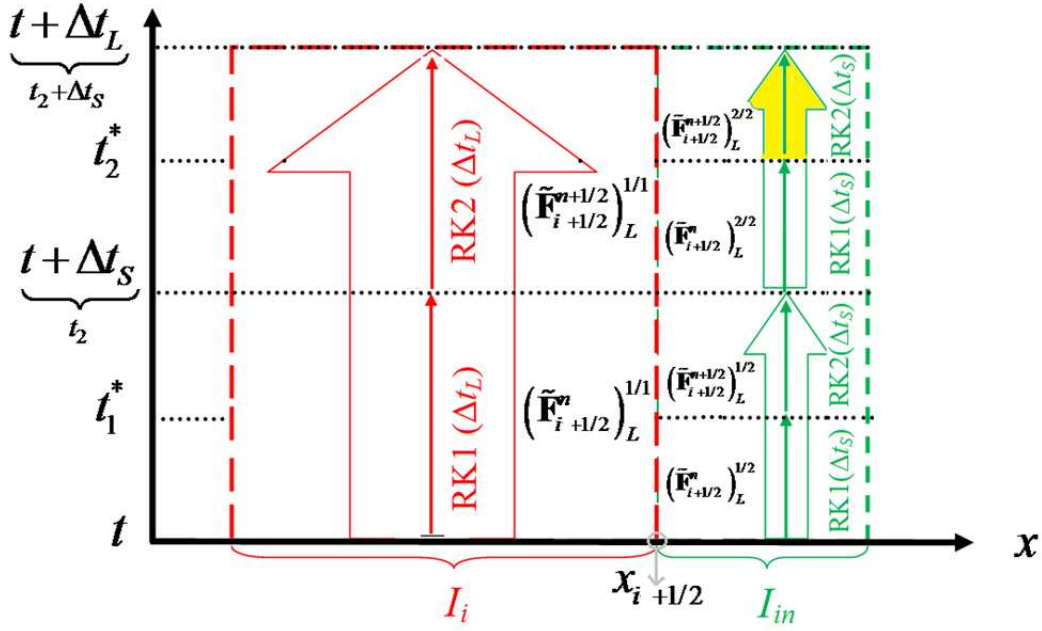


Fig. 4: History of the ‘actual’ inner RK stages of the LTS-RKDG2 calculations at the LIC I_i and the SIC I_{in} in terms of Riemann flux evaluations. Particular case (when $\Delta t_L = \Delta t$) where flux conservation reinforcement is needed and take action at the SIC within the RK2 stage of the last of LTS-RKDG2 calculation, using (25).

427

428 5.3.2 Flux conservation at interface cells

429 After achieving the LTS-RKDG2 calculations at the LIC I_i (Subsection 5.2.1) and the SIC I_{in}

430 (Subsection 5.2.2), the sum of Riemann flux quantities cumulated between times ‘ t ’ and ‘ $t +$

431 Δt_L ’ at the edge $x_{i+1/2}$ may not be equal. For instance, following the notations in Fig. 4, it may

432 happen that

$$433 \left[\left(\tilde{\mathbf{F}}_{i+1/2}^n \right)_L^{1/1} + \left(\tilde{\mathbf{F}}_{i+1/2}^{n+1/2} \right)_L^{1/1} \right]_t^{t+\Delta t_L} \neq \left[\left(\tilde{\mathbf{F}}_{i+1/2}^n \right)_S^{1/2} + \left(\tilde{\mathbf{F}}_{i+1/2}^{n+1/2} \right)_S^{1/2} \right]_t^{t_2} + \left[\left(\tilde{\mathbf{F}}_{i+1/2}^n \right)_S^{2/2} + \left(\tilde{\mathbf{F}}_{i+1/2}^{n+1/2} \right)_S^{2/2} \right]_{t_2}^{t+\Delta t_L} \quad (33)$$

434 where $(\tilde{\mathbf{F}}_{i+1/2}^n)_L^{1/1} + (\tilde{\mathbf{F}}_{i+1/2}^{n+1/2})_L^{1/1}$ is the sum of Riemann fluxes accumulated from the sole LTS-
 435 RKDG2 calculation at the LIC I_i (superscript ‘1/1’); whereas, $(\tilde{\mathbf{F}}_{i+1/2}^n)_S^{1/2} + (\tilde{\mathbf{F}}_{i+1/2}^{n+1/2})_S^{1/2}$ and
 436 $(\tilde{\mathbf{F}}_{i+1/2}^n)_S^{2/2} + (\tilde{\mathbf{F}}_{i+1/2}^{n+1/2})_S^{2/2}$ are the sum of Riemann fluxes accumulated during the first (superscript
 437 ‘1/2’) and the second (superscript ‘2/2’) LTS-RKDG2 calculations at the SIC I_{in} .

438 To alleviate this effect, flux conservation (in time) is reinforced at the SIC I_{in} and
 439 during the *final* of LTS-RKDG2 **calculation** and, more particularly, at the **RK2** stage (when
 440 the coefficients are pending one last step before reaching ‘ $t + \Delta t$ ’) [Fig. 4—right highlighted
 441 portion of the thick arrow). This can be done by exceptionally choosing the flux $(\tilde{\mathbf{F}}_{i+1/2}^{n+1/2})_S^{2/2}$ so
 442 as to ensure that the two sides of Eq. (33) remain equal, i.e.

$$443 \quad \left[(\tilde{\mathbf{F}}_{i+1/2}^{n+1/2})_S^{2/2} \right]_{t_2}^{t+\Delta t} = \left[(\tilde{\mathbf{F}}_{i+1/2}^n)_L^{1/1} + (\tilde{\mathbf{F}}_{i+1/2}^{n+1/2})_L^{1/1} \right]_t^{t+\Delta t} - \left[(\tilde{\mathbf{F}}_{i+1/2}^n)_S^{1/2} + (\tilde{\mathbf{F}}_{i+1/2}^{n+1/2})_S^{1/2} \right]_t^{t_2} - \left[(\tilde{\mathbf{F}}_{i+1/2}^n)_S^{2/2} \right]_{t_2}^{t_2^*} \quad (34)$$

444 and then proceed with the conventional evaluation for the **DG2** space operators to complete
 445 the RK2 stage.

446

447 5.4 LTS-RKDG2 algorithm on a mesh with multiple refinement levels

448 5.4.1 Computational and memory demands

449 In the GTS-RKDG2 calculation, coefficients are moved from ‘ t ’ to ‘ $t + \Delta t$ ’ in one round.
 450 Computational storage associated with this calculation (at cell I_i and for all K coefficients) are
 451 three matrices $\{\mathbf{U}_i^K\}^n$, $\{\mathbf{U}_i^K\}^{n+1/2}$ and $\{\mathbf{U}_i^K\}^{n+1}$ for storing coefficients at times ‘ t ’, ‘ t^* ’ and
 452 ‘ $t + \Delta t_{GTS}$ ’; whereas any other variables/operations are local and/or momentary.

453 Calculations of the LTS-RKDG2 are recursive and occur across 2^k rounds for cells
 454 with level ‘ k ’ of refinement ($1 \leq k \leq lev_{max}$). Nevertheless, the same allocated matrices can be
 455 used subject to re-initialization at the beginning of each round, i.e. $\{\mathbf{U}_i^K\}^n \leftarrow \{\mathbf{U}_i^K\}^{n+1}$.
 456 Nonetheless, extra *local* storage is required to facilitate the calculations at *interface cells*,

457 namely for recording the **DG2** operators at LICs, evolving sums of Riemann fluxes at
 458 *interface cells* and restoring frictionless discharge coefficients *interface cells*. Moreover,
 459 these storage demands become higher for the 2D version given the presence of an additional
 460 slope component and **DG2** operator, and two more direct neighbours.

461

462 **5.4.2 LTS-RKDG2 calculations at interface cells $\{I_i, I_{in}\}$**

463 Here, all the steps of LTS-RKDG2 calculations at $\{I_i, I_{in}\}$ are combined including the specific
 464 features relevant to hydrodynamic modelling. At time ‘ t ’, coefficients over I_i and I_{in} are
 465 available and Table 1 summarises the steps of the LTS-RKDG2 calculations for lifting
 466 coefficients of cells I_i and I_{in} to time ‘ $t + \Delta t_L$ ’ (in which subscripts ‘ L ’ and ‘ S ’ are overlooked
 467 for the coefficients and the DG2 operators).

468

469 **Table 1:** List of steps for the LTS-RKDG2 calculations at I_i (resp. I_{in}) with the LTS Δt_L (resp. $\Delta t_S =$
 470 $\Delta t_L/2$) to move its coefficients from time ‘ t ’ to time ‘ $t + \Delta t_L$ ’ in one round (resp. in two rounds).

<p>1. Start with the one round over the LIC I_i with the time step Δt_L.</p> <p>A. Detect if an IFTD is needed. If so, save the initial frictionless discharge coefficients at I_i and I_{in}; using (16) with Δt_L, do an ‘<i>actual</i>’ (reps. a ‘<i>ghost</i>’) IFTD step at I_i (resp. I_{in}) to add friction effects to the discharge coefficients in $\{\mathbf{U}_i^K\}^n$ (resp. $\{\mathbf{U}_{in}^K\}^n$). Otherwise, omit Step 1-A.</p> <p>B. Evaluate and save the Riemann flux at $x_{i+1/2}$. Then, evaluate, via (23), and save the DG2 space operators $\{\mathbf{L}_i^K\}^n$.</p> <p>C. Advance the coefficients at I_i one time stage, using (4) with the time step Δt_L, to produce $\{\mathbf{U}_i^K\}^{n+1/2}$ (i.e., ‘<i>actual</i>’ coefficients).</p> <p>D. In a similar way, i.e. via (25), advance the coefficients over I_{in} one time stage, to produce ‘<i>ghost</i>’ coefficients $\{\mathbf{U}_{in}^K\}^{n+1/2}$. Set $\{\mathbf{U}_{in}^K\}^{n+1/2} \leftarrow \{\mathbf{U}_{in}^K\}_{S,Ghost}^{n+1/2}$.</p> <p>E. If an IFTD is needed. Using (16) with Δt_L, do an ‘<i>actual</i>’ (reps. a ‘<i>ghost</i>’) IFTD step at I_i (resp. I_{in}) to add increment of friction in the discharge coefficients of $\{\mathbf{U}_i^K\}^{n+1/2}$ (resp. $\{\mathbf{U}_{in}^K\}^{n+1/2}$). Otherwise, omit Step 1-E.</p> <p>F. Evaluate and save the Riemann flux at $x_{i+1/2}$. Then, evaluate, via (23), and save the DG2 space operators $\{\mathbf{L}_i^K\}^{n+1/2}$.</p> <p>G. Advance the coefficients over I_i another time stage, using (5) with the time step Δt_L, to produce $\{\mathbf{U}_i^K\}^{n+1}$.</p> <p>H. Restore the (original) frictionless state for the coefficients $\{\mathbf{U}_i^K\}^n$ and $\{\mathbf{U}_{in}^K\}^n$ using the saved frictionless discharge coefficients in Step 1-A.</p> <p>2. Then, two rounds over the SIC I_{in} with the time step $\Delta t_S = \Delta t_L/2$.</p>

- A. Detect if an IFTD is needed. If so, using (16) with Δt_s , do an ‘*actual*’ IFTD step at I_{in} to add increment due to the friction effects to the discharge coefficients in $\{\mathbf{U}_{in}^K\}^n$. Otherwise, omit Step 2-A.
- B. Evaluate and save the Riemann flux at $x_{i+1/2}$. Then, evaluate, via (23) the **DG2** space operators $\{\mathbf{L}_{in}^K\}^n$.
- C. Advance the coefficients over I_{in} one time stage, using (4) with the time step Δt_s , to produce the ‘*actual*’ coefficients $\{\mathbf{U}_{in}^K\}^{n+1/2}$; if an IFTD is needed, using (16) with Δt_s , do another ‘*actual*’ IFTD step for $\{\mathbf{U}_{in}^K\}^{n+1/2}$.
- D. Produce ‘*ghost*’ coefficients $\{\mathbf{U}_i^K\}_{L,Ghost}^{n+1/2}$ over I_i [*i.e.*, using (29) with $\{\mathbf{U}_i^K\}^n$ from Step 1-H and the previously saved $\{\mathbf{L}_i^K\}^n$ from Step 1-B]. Set $\{\mathbf{U}_i^K\}^{n+1/2} \leftarrow \{\mathbf{U}_i^K\}_{L,Ghost}^{n+1/2}$.
- E. Evaluate and save the Riemann flux at $x_{i+1/2}$. Then, evaluate, via (23), the **DG2** space operators $\{\mathbf{L}_{in}^K\}^{n+1/2}$.
- F. Advance the coefficients over I_{in} another time stage, using (5) with the time step Δt_s , to produce $\{\mathbf{U}_i^K\}^{n+1}$.
- G. Produce time-matching ‘*ghost*’ coefficients $\{\mathbf{U}_i^K\}_{L,Ghost}^{n+1}$ over I_i (*i.e.*, using (30) with the same parameters used in (29) and by further involving $\{\mathbf{L}_i^K\}^{n+1/2}$ saved in Step 1-F).
- H. Re-initialize the coefficients at I_i and I_{in} : $\{\mathbf{U}_{in}^K\}^n \leftarrow \{\mathbf{U}_{in}^K\}^{n+1}$ and $\{\mathbf{U}_i^K\}^n \leftarrow \{\mathbf{U}_i^K\}_{L,Ghost}^{n+1}$.
- I. Do similar as Steps 2-A, 2-B and 2-C to reproduce the ‘*actual*’ coefficients $\{\mathbf{U}_{in}^K\}^{n+1/2}$.
- J. Produce, via (31), ‘*ghost*’ coefficients $\{\mathbf{U}_i^K\}_{L,Ghost}^{n+1/2}$ and reset $\{\mathbf{U}_i^K\}^{n+1/2} \leftarrow \{\mathbf{U}_i^K\}_{L,Ghost}^{n+1/2}$.
- K. Do similar as Step 2-E and Step 2-F to finally obtain the ‘*actual*’ coefficients $\{\mathbf{U}_{in}^K\}^{n+1}$.

Remark (exceptional flux conservation Step 2-L)

- L. In the case where Step 2-I – Step 2-K take action at the very last round, which is lifting the coefficients over I_{in} to ‘ $t+\Delta t$ ’, Step 2-J should be removed and the flux in Step 2-K is directly estimated by the relationship (34).

471

472 **5.4.3 Generalized LTS-RKDG2 model**

473 Following Krivodonova [24], the generalization of the LTS-RKDG2 scheme on a mesh with
 474 arbitrary depth of refinement stems from a recursive repetition of the steps in Table 1, so that
 475 to keep a “*staircase*” in time after each iteration. For simplicity, it is described for $lev_{max} = 3$
 476 in Table 2 and correspondingly in Fig. 5. Here, a total of four iterations is needed to lift the
 477 coefficients over all cells from time ‘ t ’ to time ‘ $t + \Delta t$ ’. Evidently, after round $\#k$ ($k = 1, 2, 3$
 478 and 4), the coefficients over cells with level k reaches ‘ $t + \Delta t$ ’.

479

480 **Table 2:** List of steps for LTS-RKDG2 calculations at a mesh with four refinement levels of ‘0’, ‘1’,
 481 ‘2’ and ‘3’ using respectively the LTS Δt , $\Delta t/2$, $\Delta t/2^2$ and $\Delta t/2^3$.

Round #1: advance the coefficients one LTS over all cells using Steps (1-A)—(1-H) or Steps (2-A)—(2-F). As seen in Fig. 5a, the calculation starts orderly with the cells of level ‘3’, ‘2’,

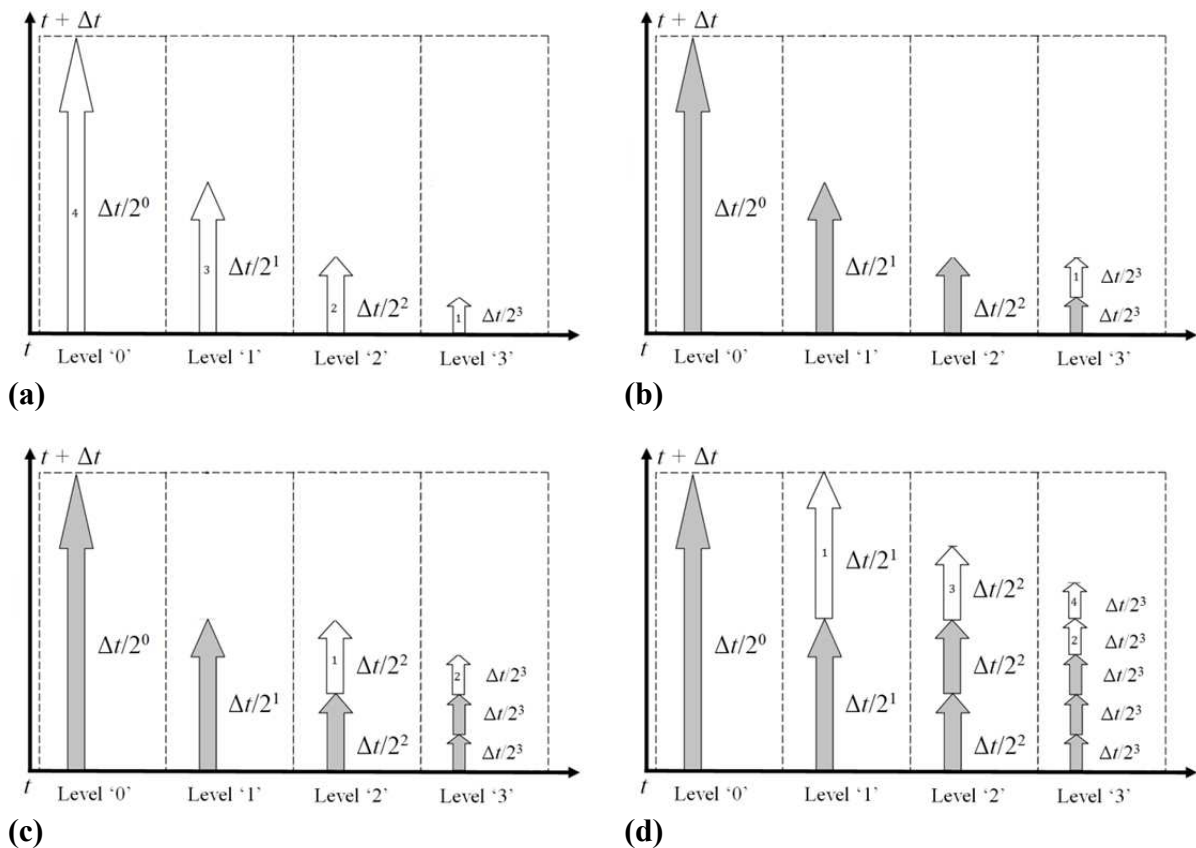
'1' and then '0' (*i.e.*, using respectively the LTS $\Delta t/2^3$, $\Delta t/2^2$, $\Delta t/2$ and Δt).

Round #2: first, advance the coefficients over cells with level '3' one LTS using Steps (2-G)—(2-K); (*i.e.*, Fig. 5b). Second, advance the coefficients over cells with level '2' one LTS using Steps (1-A)—(1-H); (*i.e.*, Fig. 5c) and revisit the cells with level '3' to further advance their coefficients another LTS using Steps (2-G)—(2-K); (*i.e.*, Fig. 5c). Fourth, advance the coefficients over cells with level '1' one LTS using Steps (2-G)—(2-K) while *enforcing flux conservation* via (34); (*i.e.*, Fig. 5d). Fifth, revisit the cells with level '3' and further advance their coefficients one more LTS using Steps (2-G)—(2-K); (*i.e.*, Fig. 5d). Sixth, revisit the cells with level '2' and further advance their coefficients one more LTS Steps (2-G)—(2-K); (*i.e.*, Fig. 5d). Finally, revisit the cells with level '3' and again advance their coefficients one more LTS using Steps (2-A)—(2-F); (*i.e.*, Fig. 5d).

Round #3: first, advance the coefficients over cells with level '3' one LTS using Steps (2-G)—(2-K); (*i.e.*, Fig. 5e). Second, advance the coefficients over cells with level '2' one LTS using Steps (2-G)—(2-K) while *reinforcing flux conservation* via (34). Finally, revisit the cells with level '3' and again advance their coefficients one more LTS using Steps (2-A)—(2-F); (*i.e.*, Fig. 5e).

Round #4: now, the remaining step is to advance the coefficients over cells of level '3' one LTS using Steps (2-G)—(2-K) while *enforcing flux conservation* via (34); (*i.e.*, Fig. 5f).

482



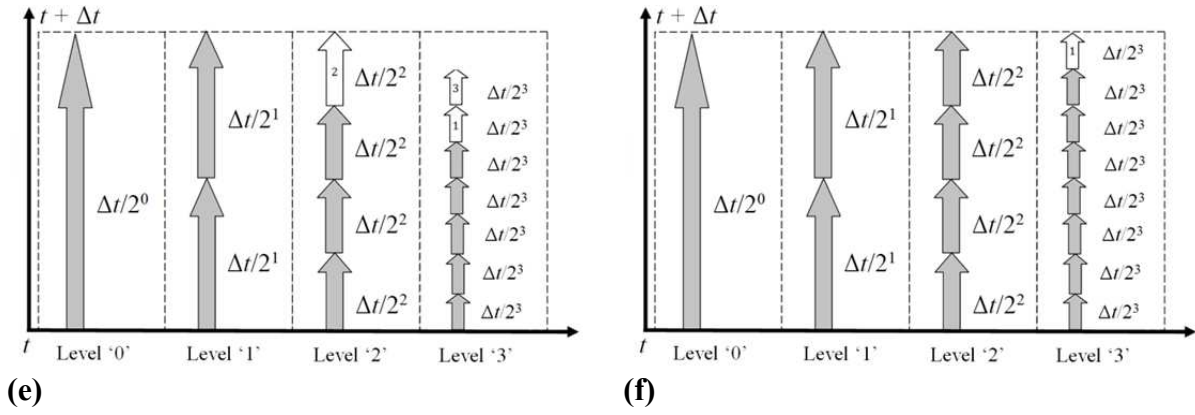


Fig. 5: Schematic description of the LTS-RKDG2 calculations over the *interface cells* relative to mesh with four levels of refinement; “**Gray arrow**” = previous step(s) and “**Blank numbered arrow**” = present step(s) in successive order.

483

484 6. LTS-RKDG2 model's verification relative to the GTS-RKDG2 model

485 The 1D and 2D formulations of the LTS-RKDG2 scheme are verified for two non-uniform
 486 mesh configurations, refereed hereafter to as ‘*mesh-3LTSs*’ and ‘*mesh-4LTSs*’, which
 487 respectively involve ‘3’ and ‘4’ levels of local spatial-temporal discretization-scales (*i.e.*,
 488 $lev_{\max} = 2$ and $lev_{\max} = 3$, respectively). On the former mesh the LTS-RKDG2 framework
 489 coordinates the LTSs $\{\Delta t, \Delta t/2, \Delta t/4\}$ while it coordinates the LTSs $\{\Delta t, \Delta t/2, \Delta t/4, \Delta t/8\}$ on
 490 the latter mesh. Selected benchmark tests are employed to investigate the performance of the
 491 LTS-RKDG2 scheme (*i.e.*, 1D and/or 2D versions on both ‘*mesh-3LTSs*’ and ‘*mesh-4LTSs*’)
 492 with respect to the traditional GTS-RKDG2 scheme, while discussing/identifying several
 493 issues pertaining to computational hydraulics and quantifying the runtime saving (*i.e.*, the
 494 ratio ‘runtime GTS’/‘runtime LTS’). By default, transmissive (numerical) boundary
 495 conditions are used in the both RKDG2 models unless otherwise mentioned for specific test
 496 cases.

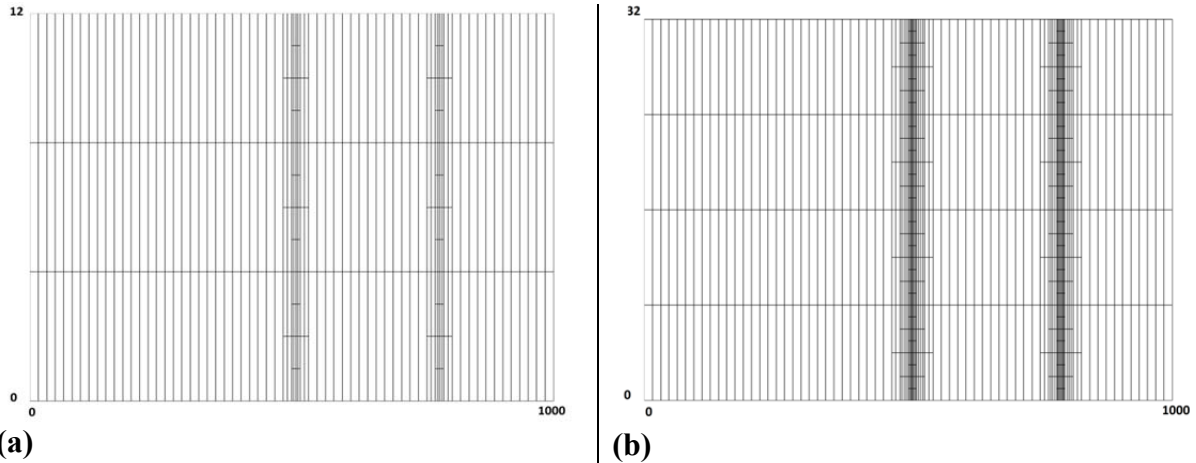


Fig. 6: Transcritical flow over a hump with shock. 2D domains and meshes with local refinement around the point of transcritical flow and the local of the water jump; **(a)** $lev_{max} = 2$ and **(b)** $lev_{max} = 3$.

497

498 **6.1 Steady transcritical flow over topography with shock**

499 This test investigates moving steady transcritical flow over non-flat topography with a shock.

500 It is usually employed to demonstrate the capability of a numerical method to converge

501 towards a steady state, accurately balance the flux gradient with the topography gradient, and

502 capture transcritical flow transitions and water jumps. The channel is 1000m long with a

503 hump-shape topography located between $x = 125\text{m}$ and $x = 875\text{m}$ [38]. Inflow (physical)

504 boundary condition is imposed through a unit discharge of $20\text{m}^2/\text{s}$ and the (physical) outflow

505 boundary is a water level of 7m. Under these conditions, a steady transitional flow takes

506 place where the flow changes from subcritical to supercritical at $x = 500\text{m}$. Downstream of

507 the topography, a hydraulic jump occurs as the flow regime restores to subcritical. A

508 simulation starts from an initial water height of 9.7m and is desired to stop after a relatively

509 long time evolution (*i.e.*, $t = 2000\text{s}$). Simulations are done using the 1D and 2D versions of

510 the GTS-RKDG2 and LTS-RKDG2 schemes. The 1D and 2D mesh characteristics are listed

511 in Table 3; the 2D domains and associated mesh-refinement are described in Fig. 6, while the

512 level of refinement used for the 1D meshes are marked in Fig. 7 (the *grey* diamond marker

513 within the upper panel).

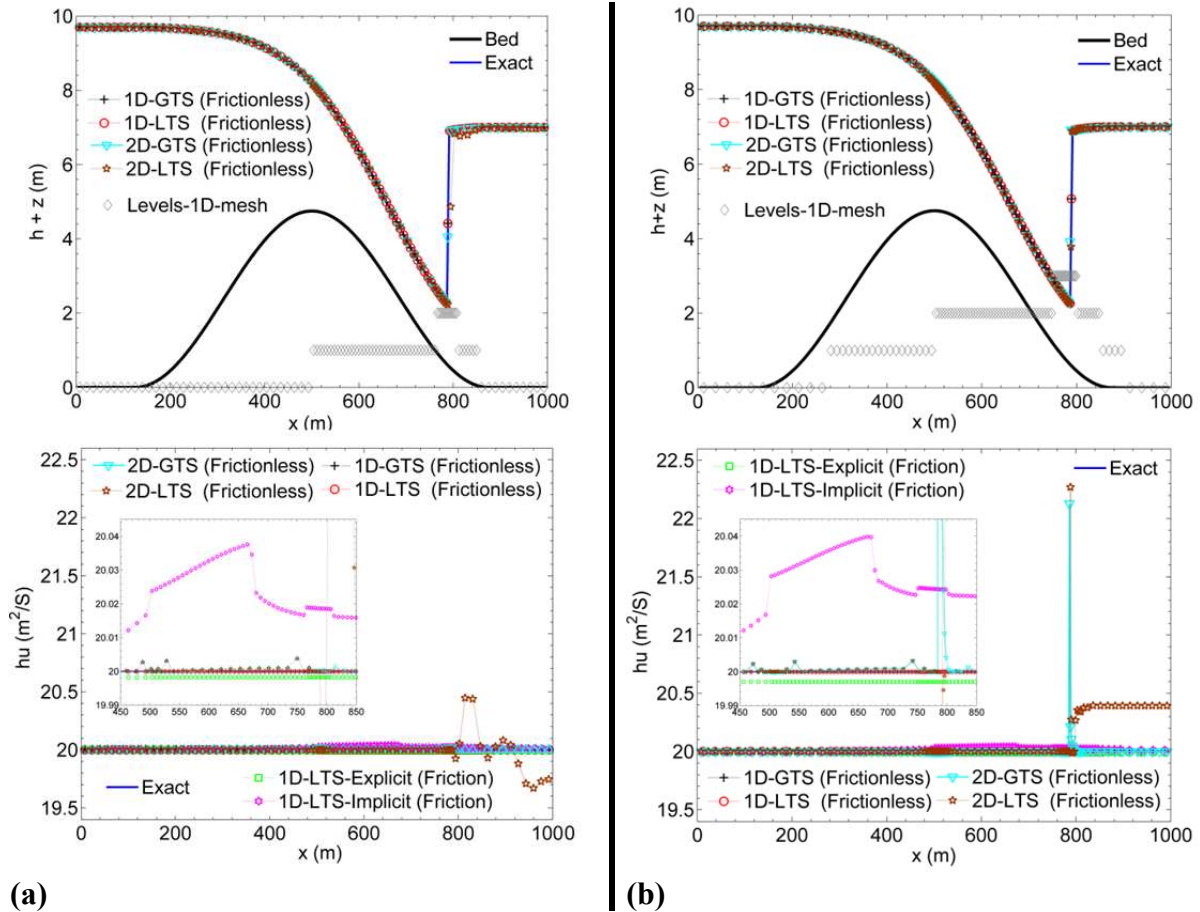


Fig. 7: Transcritical flow over a hump with shock. LTS-RKDG2 calculations vs. GTS-RKDG2 calculations compared with the analytical solution; **(a)** $lev_{max} = 2$ and **(b)** $lev_{max} = 3$.

514

515

516

517

518

519

520

521

522

523

524

525

At first, the channel's bed is assumed frictionless. Fig. 7a and Fig. 7b display the corresponding steady state profiles acquired by the 1D and 2D versions of the RKDG2 solvers on *mesh-3LTSs* and *mesh-4LTSs*, respectively. It can be seen that the numerical water depths predictions match very well the analytical solution. For the momentum conservation predictions, in terms of steady discharge, the expected conservative state is reached by all the 1D-RKDG2 variants (GTS- and LTS-, and on both meshes) and the 2D-GTS-RKDG2 variant relative to *mesh-3LTSs*. In contrast, the 2D-LTS-RKDG2 variant shows deficit in achieving an fully conservative steady discharge profile; notable also, both 2D-RKDG2 (GTS- and LTS-) models on *mesh-4LTSs* shows the localized discharge spike (Fig. 7b) at the jump's location, which is suspected to occur as a result of a redundant call to the slope-limiter function [39]. However, these side effects remain rather localized and do not appear to affect

526 the whole simulations. These findings indicate that the current LTS-RKDG2 model can
 527 maintain the well-balanced property [29] in the 1D formulation but tend to locally disturb
 528 momentum conservation in the 2D formulation increasingly with more refinement levels.

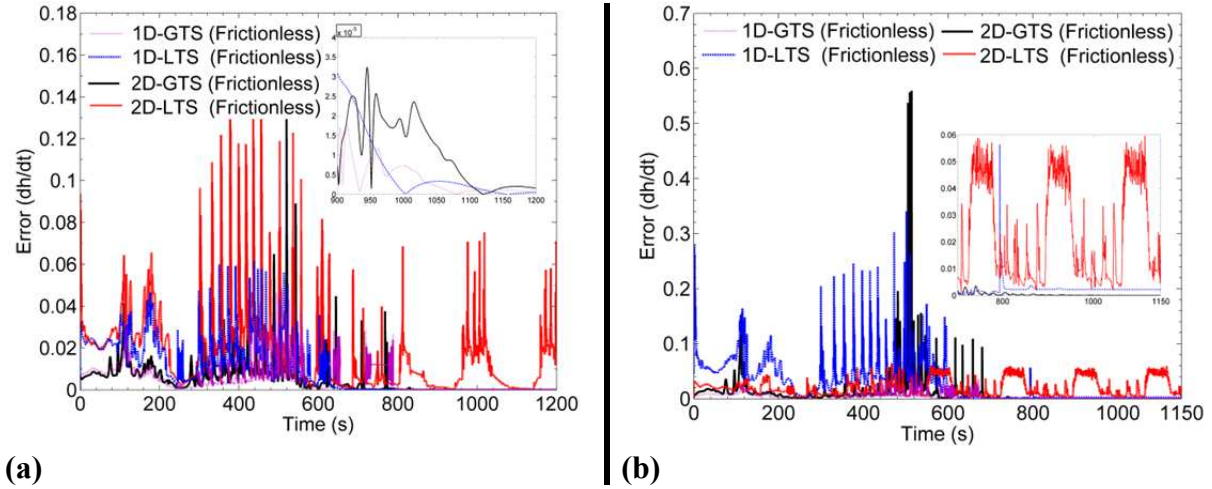


Fig. 8: Transcritical flow over a hump with shock. LTS-RKDG2 calculations vs. GTS-RKDG2 convergence rates; **(a)** $lev_{max} = 2$ and **(b)** $lev_{max} = 3$.

529
 530 Up to $t = 2000s$, the LTS-RKDG2 model is spotted to reduce the GTS-RKDG2
 531 runtime up to roughly 2X in 1D and 1.5X in 2D (see Table 3). In terms of convergence rates,
 532 the L^2 -errors defined by the ‘variations of the water depth between two successive iterations’
 533 were monitored and are illustrated in Fig. 8 (*i.e.*, relative to the output time when the L^2 -error
 534 of the 2D-GTS-RKDG2 variant became $\leq 10^{-8}$). As shown in Fig. 8a, the convergence error
 535 produced by 2D-LTS-RKDG2 variant on *mesh-3LTSs* is seen to alternate steadily; whereas
 536 the errors acquired by the other variants appear to follow the expected exponential decay (see
 537 the zoom-in portion within the upper-right in Fig. 8a). However, on *mesh-4LTSs* (*i.e.*, Fig.
 538 8b) the 1D-LTS-RKDG2 variant’s error appear to stagnate after a certain time while the 2D-
 539 LTS-RKDG2 variant’s error produces again an alternating pattern (see the zoom-in portion
 540 within the upper-right in Fig. 8b). With these results, it appears that the RKDG2 framework
 541 risk losing its ability to delivering exponential convergence rates. It can be therefore argued
 542 that the present LTS-RKDG2 framework may compromise with either a delay or stagnation

543 in reaching convergence for steady flow simulations (also depending on the dimensionality of
 544 the formulation and/or the depth of refinement levels [Fig. 8]).

545

546 **Table 3:** Mesh configurations and runtime ratios after 2000s for test-case 6.1

<i>Simulation case</i>	1D		2D	
<i>Level of refinement</i>	2	3	2	3
<i>Baseline mesh</i>	62	40	62×3	64×4
<i>Domain</i>	[0;1000]	[0;1000]	[0;1000]×[0;12]	[0;1000]×[0;32]
<i>Runtime ratio (GTS/ LTS)</i>	1.9X	2.3X	1.6X	1.5X

547

548 Secondly, this test case is used to further point out the inconvenience of the IFTD
 549 when solely implemented in conjunction with the LTS-RKDG2 scheme. Therefore, the 1D-
 550 LTS-RKDG2 method is reconsidered with a Manning factor of $0.033 \text{ s/m}^{1/3}$; the simulations
 551 are remade on the same non-uniform meshes (in Table 3) but now with a focus on comparing
 552 the IFTD discretization (i.e., time-dependent) vs. the explicit friction term discretization (i.e.,
 553 independent of the time-step). The solution to the momentum equation, in terms of steady
 554 discharge numerical result, is appended within the discharge plots of Fig. 7a and 7b. As
 555 outlined before (Subsection 5.3.1), the use of the IFTD with the LTS-RKDG2 tends to
 556 magnify the impact of the IFTD by increasing the amount of numerical diffusion manifesting
 557 itself in form of disturbance in the well-balanced property of the RKDG2 scheme. Further,
 558 this side-effect is observed to increase in line with either an increase in the Manning factor
 559 (herein, zoom-in of discharge illustrations within Figs. 7a and 7b contains the results relative
 560 to the highest value of n_M that was tested, i.e., $n_M = 0.033 \text{ s/m}^{1/3}$) or in the level of LTS (in
 561 that, the LTS-RKDG2-IFTD's discharge prediction in Fig. 7a is less diffusive than the one in
 562 Fig. 7b). As anticipated, the discharge solution reproduced by the LTS-RKDG2 scheme with
 563 the explicit friction discretization remain comparatively unaffected – despite an insignificant
 564 drop that is believed to occur as a results of coarsening the mesh at the boundary and also,
 565 perhaps, due to the heuristic nature of Manning's formula. These results justify the

566 motivation to use the proposed hybrid explicit-implicit friction term discretisation (employed
 567 from now on for the test cases 6.2-6.5).

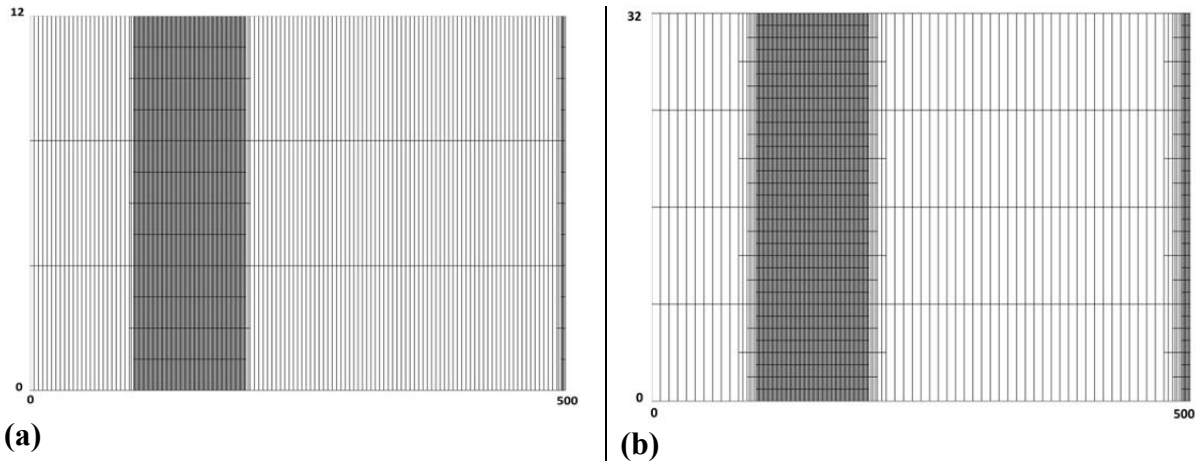


Fig. 9: Wet/dry front advancing and recessing over a rough topography. 2D domains and mesh configurations with local refinement around the steepest topogprahy gradient and at inflow boundary; **(a)** $lev_{max} = 2$ and **(b)** $lev_{max} = 3$.

568

569 **6.2 Wet/dry front advancing and recessing over a rough topography**

570 This synthetic tidal wave case was initiated by Heniche et al. [40] and is a commonly used
 571 test case to verify the stability and robustness of a numerical model when reproducing the
 572 movement of a wet/dry front over an uneven and rough topography. It can be regarded as a
 573 tidal wave running up and down over sloping beach in a 1D domain [0m; 500m] with a slope
 574 of -0.001 over [0m; 100m], -0.01 over]100m; 200m] and -0.001 over]200m ;500m]. The
 575 friction effects are quite significant as they associate to a Manning coefficient of $n_M = 0.03$.
 576 The flow is initially still with a constant surface elevation of 1.75m. The eastern end of the
 577 domain ($x = 500m$) is assumed to be the inlet where the varying water depth reads

$$578 \quad h(500, t) = 1 + 0.75 \cos\left(\frac{2\pi t}{T}\right) \quad (35)$$

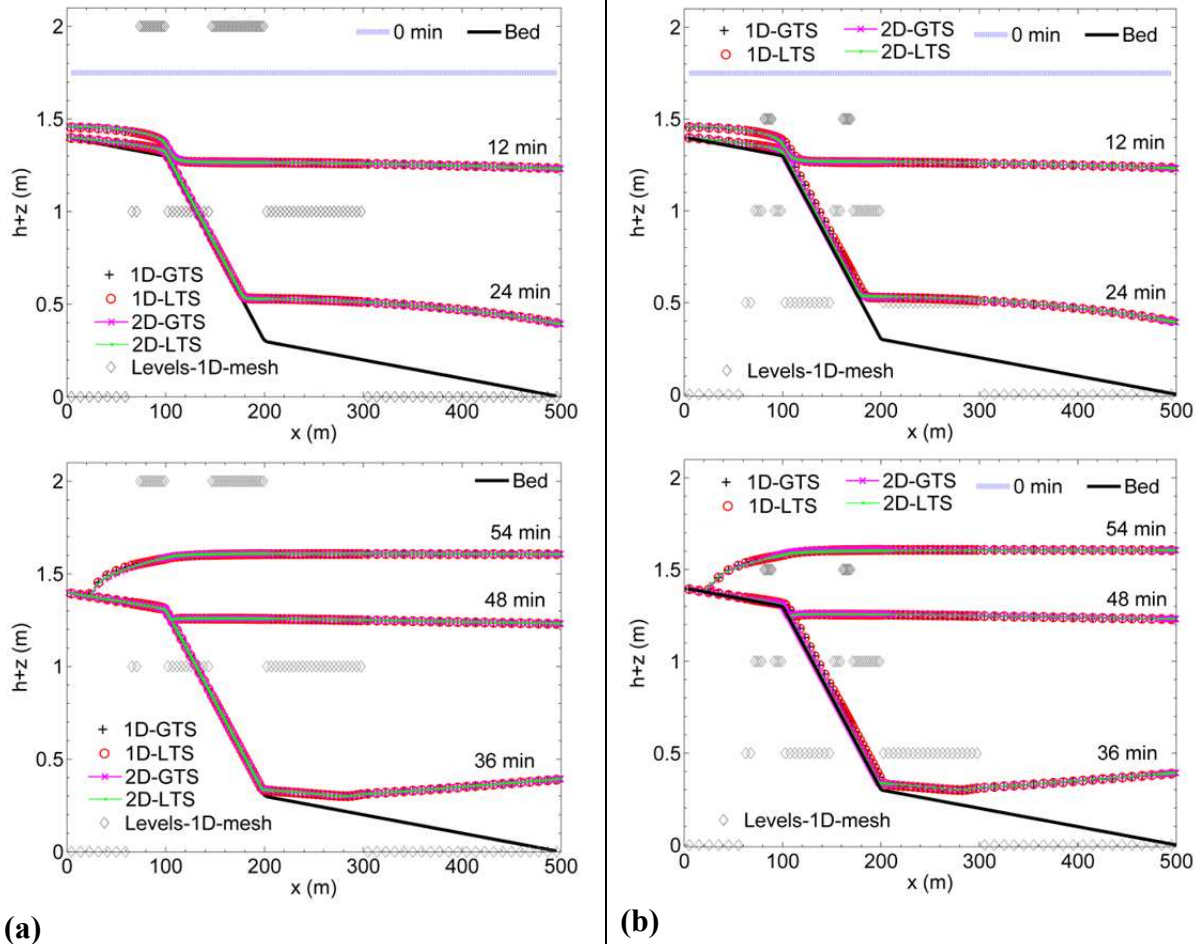
579 which mimics a tidal wave with $T = 60min$ representing the period of a tidal cycle. The
 580 western end of the domain is a standing solid wall.

581 **Table 4:** Mesh configurations and runtime ratios after 60 min for test-case 6.2

<i>Simulation case</i>	1D		2D	
<i>Level of refinement</i>	2	3	2	3

<i>Baseline mesh</i>	62	50	124×3	62×4
<i>Domain</i>	[0;500]	[0;500]	[0;500]×[0;12]	[0;500]×[0;32]
<i>Runtime ratio (GTS/ LTS)</i>	1.4X	2.5X	1.18X	1.23X

582



(a) **(b)**
Fig. 10: Wet/dry front advancing and recessing over a rough topography. LTS-RKDG2 calculations vs. GTS-RKDG2 calculations **(a)** $lev_{max} = 2$ and **(b)** $lev_{max} = 3$.

583

584

585

586

587

588

589

590

591

1D and 2D, LTS- and GTS-, RKDG2 runs on the meshes configurations described in Table 4 are performed. The employed meshes, of type *mesh-3LTSs* and *mesh-4LTSs*, are displayed in Fig. 9 for the 2D case whereas for 1D case the meshes properties are marked within Fig. 10 (for convenience, the marker's plots in Fig. 10b are shrank by a factor of 0.5). The simulations output time is 60min (*i.e.*, one tidal cycle). The LTS- and GTS- RKDG2 solutions of the advancing and recessing shoreline, at $t = 0, 12, 24, 36, 48$ and 54min are presented in Fig. 10a and Fig. 10b, respectively, on *mesh-3LTSs* and *mesh-4LTSs*. Apparently, here, the LTS-RKDG2 and GTS-RKDG2 predictions agree very closely and also

592 match those presented in literature (*e.g.*, in [27]). Nevertheless, for this test, as summarizes
 593 Table 4, the LTS-RKDG2 is found less costly than the GTS-RKDG2; namely the relative
 594 saving in runtime is about 1.2X in 2D and reached 2.5X for the 1D case on *mesh-4LTSs*.

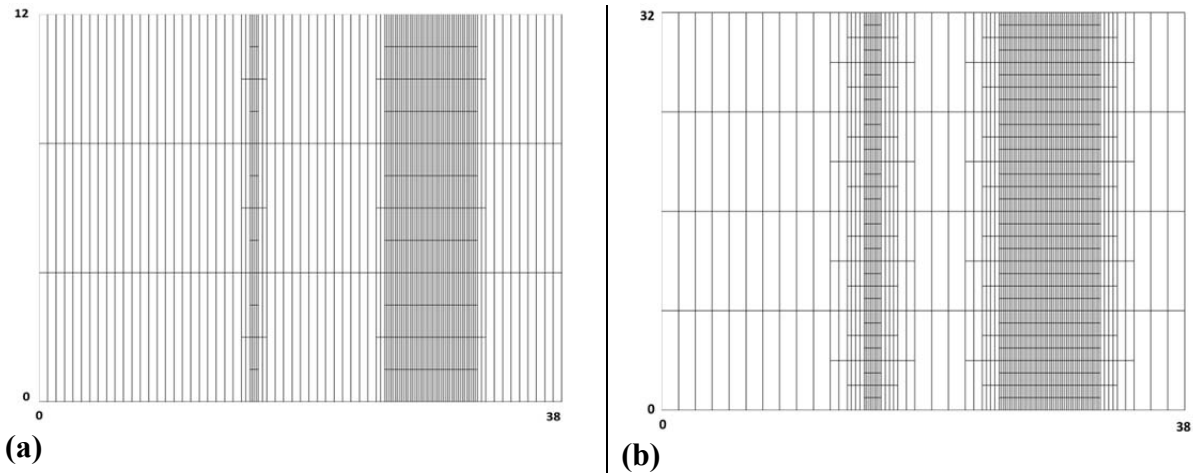


Fig. 11: Dam-break flow interacting with a triangular obstacle. 2D domains and mesh configurations with refinement at the local of the initial dam and around the triangular obstacle; **(a)** $lev_{max} = 2$ and **(b)** $lev_{max} = 3$.

595

596 **6.3 Dam-break wave interacting with a triangular obstacle**

597 The RKDG2 schemes are here assessed by replicating an experimental test case from the
 598 CADAM project [41]. It consist of a violent breaching wave propagating over an initially dry
 599 and rough floodplain, overtopping a triangular obstacle and then interacting with it. The
 600 length of the domain is 38m; the initial condition is a still water state of 0.75 m held by an
 601 imaginary dam (located at $x = 15.5\text{m}$) and a dry floodplain downstream of the dam (see Fig.
 602 12). For this problem, measured time histories of the water depth are available at point G10,
 603 G11, G13 and G20 that are respectively located 10 m, 11 m, 13 m and 20 m downstream of
 604 the dam's location. The friction effects are associated to a Manning factor of 0.0125.

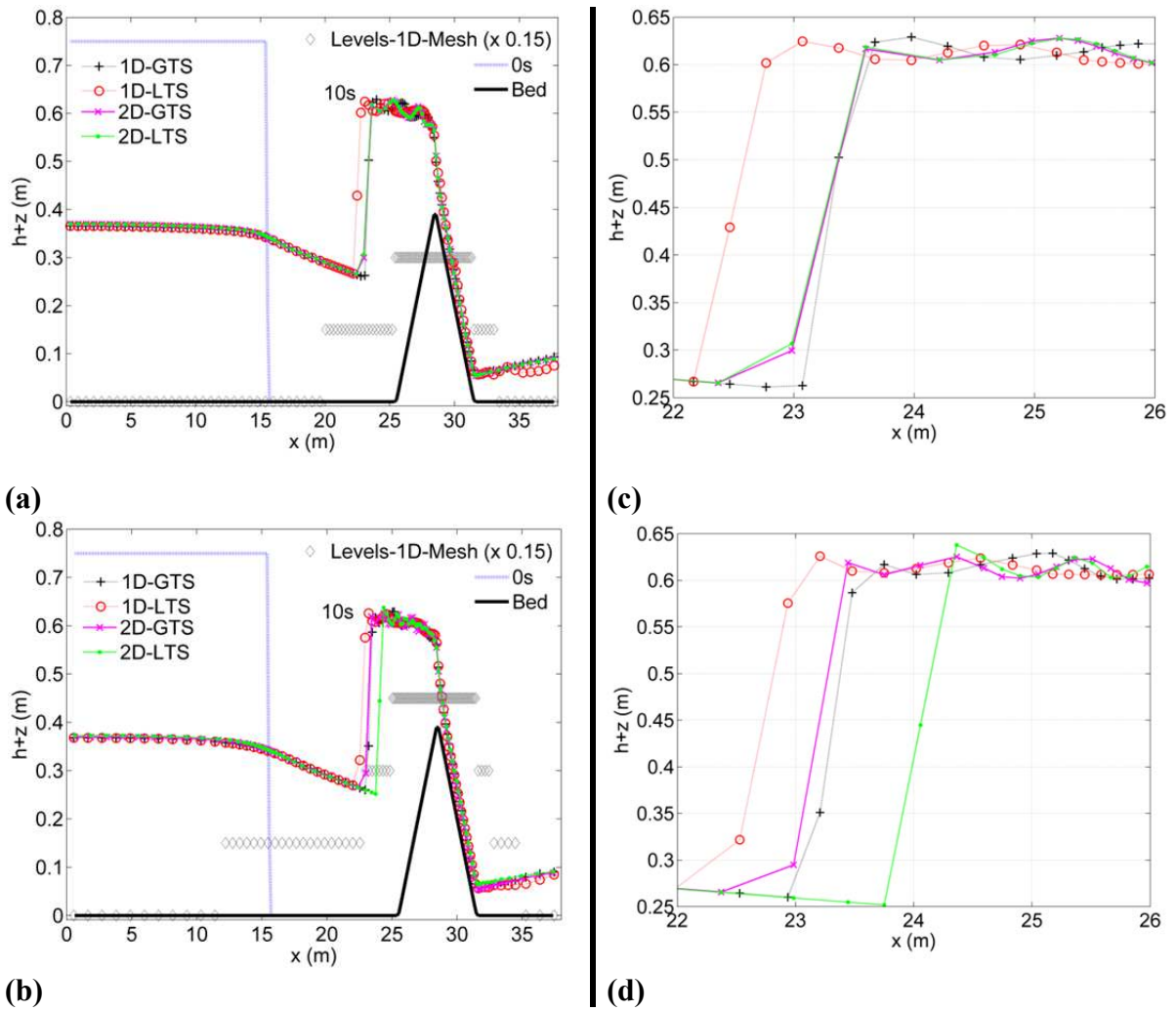


Fig. 12: Dam-break flow interacting with a triangular obstacle at $t = 10s$. LTS-RKDG2 calculations vs. GTS-RKDG2 water-surface profiles; **(a)** $lev_{max} = 2$ and **(b)** $lev_{max} = 3$, **(c)** zoom in around the shock wave $lev_{max} = 2$, and **(d)** zoom in around the shock wave $lev_{max} = 3$.

605

606

607

608

609

610

611

612

613

614

The upstream boundary is a solid wall while free outflow condition is permitted at the downstream boundary. Simulations are executed using the LTS- and GTS- RKDG2 variants with the mesh setups described in Table 5; *mesh-3LTSs* and *mesh-4LTSs* used for the 2D case are viewed in Fig. 11; for the 1D case, the meshes are described within Fig. 12 (i.e. the markers). The output simulation time is $t = 35s$. A view of the free-surface elevation longitudinal profiles predicted by the all RKDG2 versions is available in Fig. 12 at time $t = 10s$. Moreover, Fig. 13 contains the predicted time histories that are seen to favourably track with the measured profiles. As previews Fig. 12, the generated wave front propagates to the obstacle, climbs up and overtops the obstacle, creates a shock-wave moving to the upstream

615 wall. A magnified view on the shock-capturing ability of the RKDG2 models (in Fig. 12c and
616 Fig. 12d) shows a remarkable agreement between the 2D models (GTS- and LTS) and the
617 1D-GTS models for the simulations involving ‘3’ refinement levels. However, this agreement
618 appears to slightly decline when ‘4’ levels were considered in the simulations; namely for the
619 2D-LTS-RKDG2 variant that predicted a delay in the capture of the shock as compared to the
620 GTS versions (in 1D and 2D). As to the 1D-LTS-RKDG2, here, it displays a tendency to
621 accelerate shock-capturing in all simulations. These implications thus favour the use of the
622 2D-LTS-RKDG2 model on *mesh-3LTSs* over any other LTS variant for this test. Taken as
623 whole, all LTS- and GTS- RKDG2 variants successfully survived this benchmark showing
624 slight differences throughout the whole simulations (see Fig. 13), which seem to have
625 inconsequential effects on the stability of the LTS-RKDG2 models. The over-predictive
626 aspect delivered by the RKDG2 predictions at G20 has no concern with the numerical
627 algorithms; it is usually credited to the fact that the wave pattern downstream of the obstacle
628 becomes highly complex and unstable and so the hydrostatic assumption of the shallow water
629 equations is no longer valid. In terms of runtime saving, as shows Table 5, the use of LTS-
630 RKDG2 scheme is on average 1.3X and 1.18X for the 1D and the 2D versions, respectively.

631 **Table 5:** Mesh configurations and runtime ratios after 35s for test-case 6.3

<i>Simulation case</i>	1D		2D	
<i>Level of refinement</i>	2	3	2	3
<i>Baseline mesh</i>	63	35	62×3	31×4
<i>Domain</i>	[0;38]	[0;38]	[0;38]×[0;12]	[0;38]×[0;32]
<i>Runtime ratio (GTS/ LTS)</i>	1.32X	1.36X	1.16X	1.21X

632

633

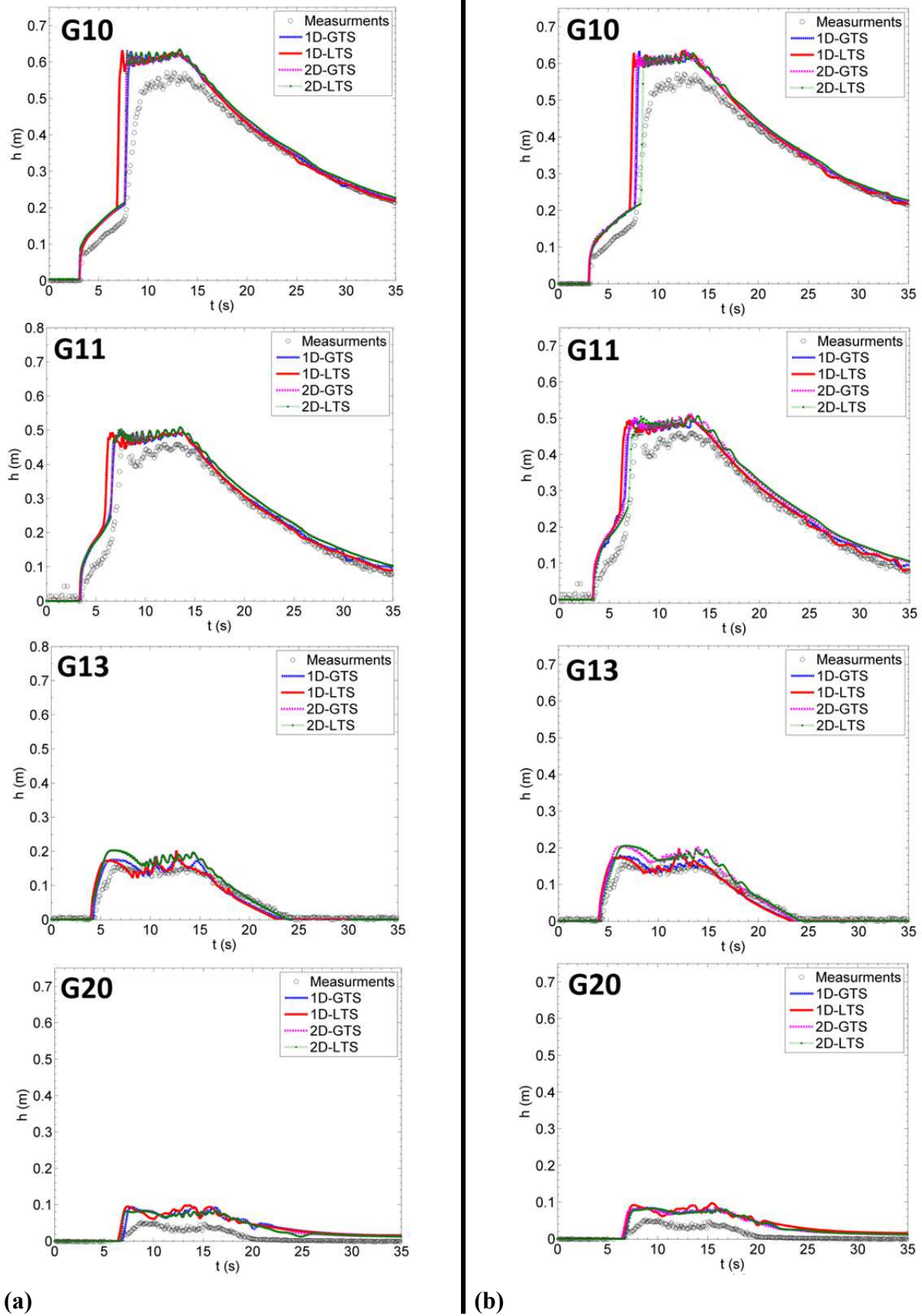


Fig. 13: Dam-break flow interacting with a triangular obstacle. Time histories produced by the RKDG2 calculations compared with measured data; **(a)** $lev_{max} = 2$ and **(b)** $lev_{max} = 3$.

635 **6.4 2D smooth oscillatory flow in a parabolic bowl with friction**

636 Sampson's 2D analytical test [42] is employed to study second-order mesh convergence for
637 the RKDG2 schemes on the non-uniform mesh configuration (both LTS- and GTS- versions
638 in 2D) and further assess their performance in handling frictional flow with wetting and
639 drying over irregular topography. This test is featured by a constantly-moving wet/dry
640 (circular) shoreline inside the 2D parabolic terrain $z(x, y) = h_0(x^2 + y^2)/a^2$, where h_0 and a
641 are constants. The energy dissipation, due to friction, is assumed proportional to the
642 magnitude of the discharge and can be integrated by altering C_f to $C_f = h\tau / \sqrt{u^2 + v^2}$, where
643 τ represents a bed-friction parameter. A 2D analytical solution can be obtainable when
644 $\tau < p$, where $p = \sqrt{8gh_0/a^2}$ represents the peak amplitude. With this setting, the exact
645 solution follows

$$646 \begin{cases} \eta(x, y, t) = h_0 - \frac{B^2}{2g} e^{-t\tau} - \frac{B}{g} e^{-t\tau/2} \left\{ \left[\frac{\tau}{2} \sin(wt) + s \cos(wt) \right] x + \left[\frac{\tau}{2} \cos(wt) + s \sin(wt) \right] y \right\} \\ u(t) = B e^{-t\tau/2} \sin(wt) \\ v(t) = -B e^{-t\tau/2} \cos(wt) \end{cases} \quad (36)$$

647 Where B is a velocity constant and $w = \sqrt{p^2 - \tau^2} / 2$. Herein, the 2D domain is chosen to be [-
648 5000; 5000]² and the constants are set to $h_0 = 10\text{m}$, $B = 5\text{m/s}$, $a = 3000\text{m}$ and $\tau = 0.009 \text{ s}^{-1}$,
649 which is a relatively high friction factor (as $\tau = 0.009 < 0.0093 = p$). For the frictionless case
650 (i.e., $\tau = 0$), the flow would oscillates indefinitely with a period cycle of $T = 2\pi/w \approx$
651 1345.7104s. But with the inclusion of friction effects the oscillatory flow is expected to cease
652 into the state $\eta(x, y, \infty) = h_0$, $u(\infty) = 0$ and $v(\infty) = 0$.

653 The initial conditions for the flow variables are obtained from (36), evaluated at $t =$
654 0s, and the output time is $t = 2Ts$. Since the flow does not reach the 2D domain's boundaries,
655 any boundary condition can be specified. To undergo the mesh convergence study, two series
656 of simulations are run on meshes of type *mesh-3LTSs* and *mesh-4LTSs*. The baseline mesh

657 details for the first and second series of simulations are, respectively, listed in Table 6 and
 658 Table 7. Qualitatively, however, to save space, we only show the mesh patterns associated to
 659 the coarsest baseline mesh (*i.e.*, Fig. 14) used in each series of simulations; the corresponding
 660 initial contour map of the water depth is also illustrated in Fig. 14.

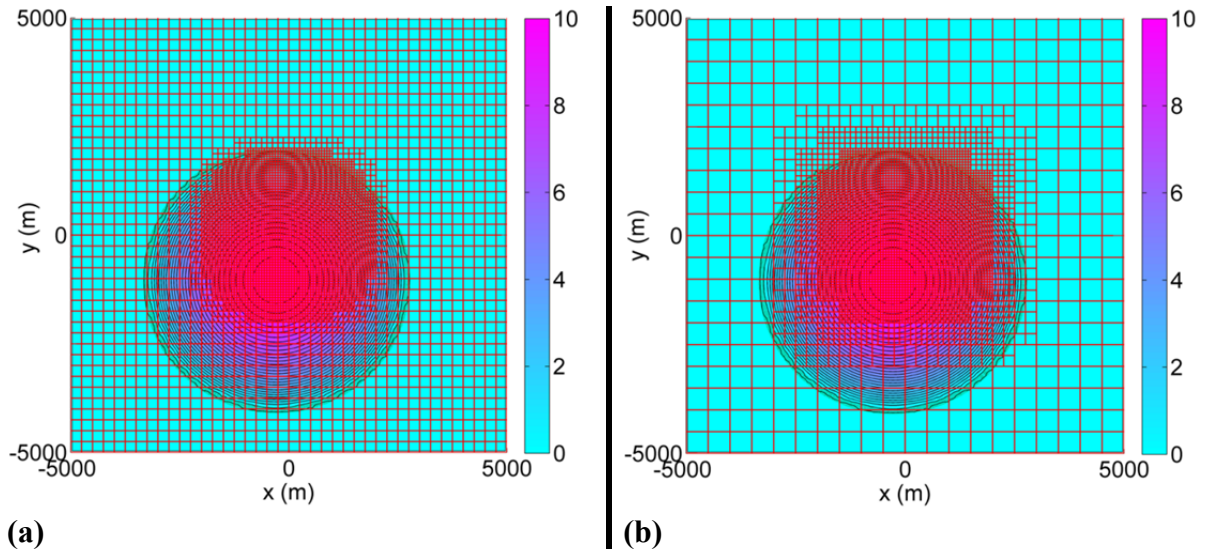


Fig. 14: Oscillatory flow in a parabolic bowl with friction. Initial water-depth condition, 2D domain and mesh configurations with a refined portion; **(a)** baseline mesh 40×40 with $lev_{max} = 2$ and **(b)** baseline mesh 20×20 with $lev_{max} = 3$.

661

662 The outputs of the 2D-LTS-RKDG2 and 2D-GTS-RKDG2 versions, at the time $T/2s$, are
 663 used to calculate the L^2 -errors (and associated and L^2 -orders) along the x -direction centreline.

664 The quantitative results are summarized in Table 6 and Table 7, which also list the runtime

665 ratios respective to the output time $t = 2Ts$. As indicates Tables 6, both GTS- and LTS-

666 models are noted to acquire second-order mesh-convergence on the mesh of type *mesh-*

667 *3LTSs*. But for these runs, the 2D-LTS-RKDG2 variant is noted to be more expensive than

668 the 2D-GTS-RKDG2 variant. In contrast, as point out Table 7, the 2D-LTS-RKDG2 scheme

669 provide relative reduction in the runtime cost by a mean factor of 1.2X for the case involving

670 a mesh of type *mesh-4LTSs*. However, on the latter setting, the RKDG2 schemes (both LTS-

671 and GTS-) do not seem to achieve second-order convergence one the latter mesh patterns.

672 Remarkably, these results suggest that increasing the deepness of spatial refinement levels –

673 although works in the favour of efficiency – pays off accuracy as such [17]; despite the
674 complementary effects (*e.g.*, flux reinforcement in time) associated with the LTS algorithms.
675 Thus, the question of how to comprehensively ensure conservative data (and fluxes) transfer
676 and recovery across the heterogeneous spatial and/or temporal scales on-uniform meshes is
677 yet to be resolved (note that, on uniform meshes, the RKDG2 delivers second-order
678 convergence rates for this test case [16, 35]).

679
680 **Table 6:** Case of $Lev_{max} = 2$. L^2 -errors and -orders evaluated at $T/2s$ and runtime ratios at $2Ts$.

Baseline Mesh	2D-GTS-RKDG2				2D-LTS-RKDG2				Runtime ratio (GTS/ LTS)
	Error(h)	Order(h)	Error(hu)	Order(hu)	Error(h)	Order(h)	Error(hu)	Order(hu)	
40×40	4.50e-03	--	6.26e-04	--	3.91e-03	--	3.91e-04	--	0.18X
80×80	3.41e-04	1.89	1.25e-04	2.31	3.03e-04	1.87	9.77e-05	2.00	0.60X
160×160	2.09e-05	2.16	1.69e-05	2.88	2.03e-05	2.12	1.40e-05	2.80	0.86X

681

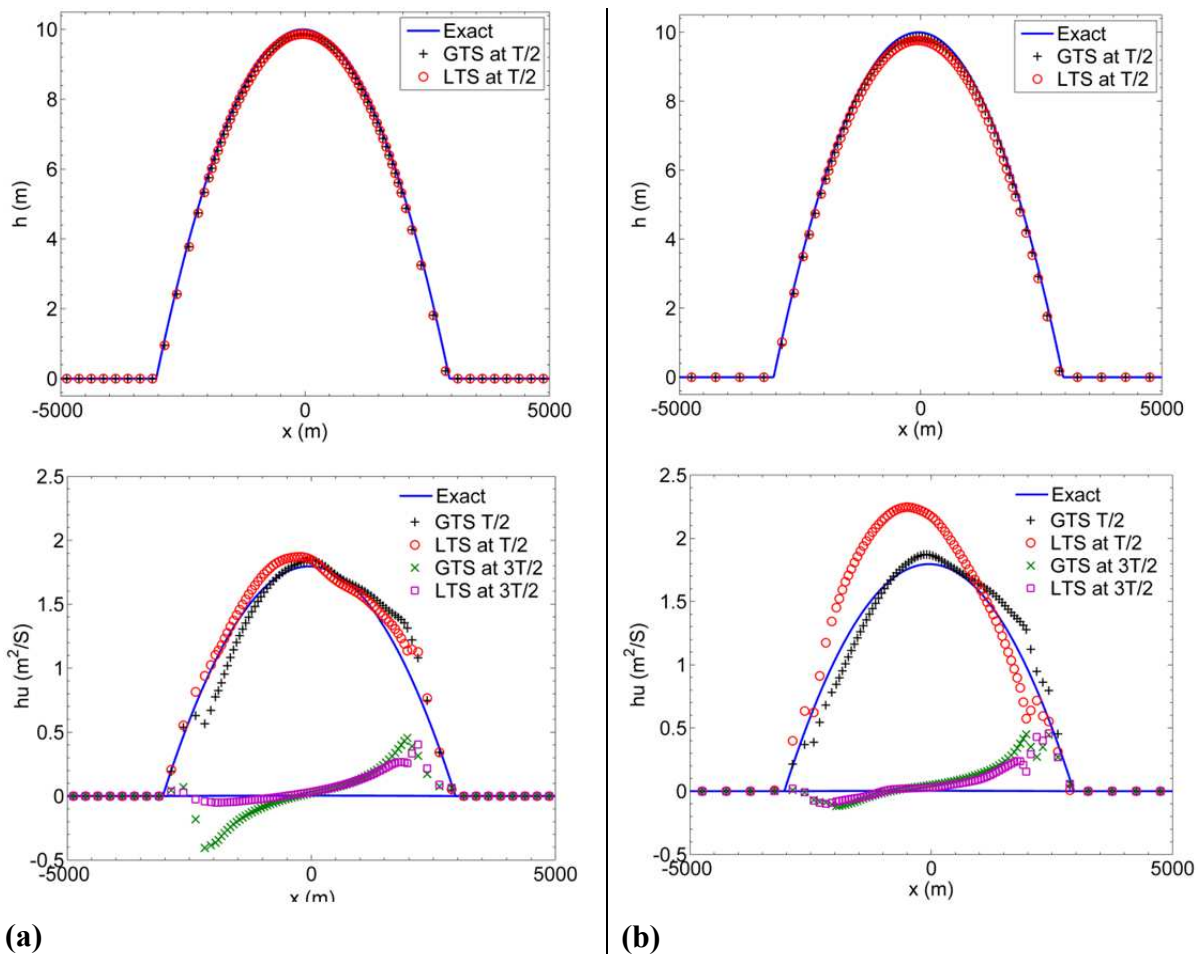
682 **Table 7:** Case of $Lev_{max} = 3$. L^2 -errors and -orders evaluated at $T/2s$ and runtime ratios at $2Ts$.

Baseline Mesh	2D-GTS-RKDG2				2D-LTS-RKDG2				Runtime ratio (GTS/ LTS)
	Error(h)	Order(h)	Error(hu)	Order(hu)	Error(h)	Order(h)	Error(hu)	Order(hu)	
20×20	1.19e-04	--	5.76e-04	--	1.74e-04	--	1.59e-03	--	1.3X
40×40	5.01e-05	1.25	2.50e-04	1.20	8.51e-05	1.03	7.67e-04	0.97	1.21X
80×80	2.08e-05	1.26	4.47e-05	2.50	4.01e-05	1.08	3.72e-04	1.04	1.25X

683

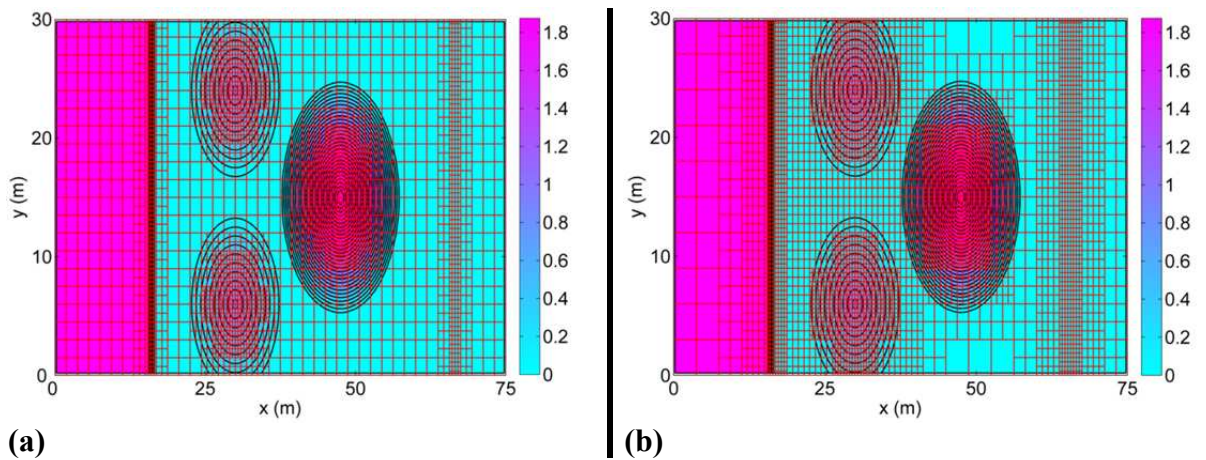
684 Fig. 15 compares the numerical predictions with the analytical solution along the x -direction
685 centreline for the water depth variable at $T/2s$ (upper panel) and the discharge variable at $T/2s$
686 and $3T/2s$ (lower panel). Fig. 15 supports the aforementioned argument (revealed in Table 6
687 and Table 7); the predictions delivered by the all RKDG2 schemes (LTS- and GTS-) using
688 less level of refinement (in space for the GTS and further in time for the LTS version) match
689 much better the exact solution. Remarkable also, the 2D-LTS-RKDG2 discharge prediction is
690 much more deviated from the 2D-GTS-RKDG2 on the mesh with the more refinement levels;
691 thus suggestive of a cumulative effect occurring further from the temporal transfer of
692 information (in the 2D-LTS-RKDG2) across the levels of resolution. In terms of modelling
693 the moving wet/dry shoreline, all RKDG2 schemes successful tracked the constantly-

694 vanishing velocity zone (see discharge plots at $3T/2$ s in Fig. 15 [lower panel]) with no signs
 695 of a conflict between LTS and wetting and drying.



(a) (b)
Fig. 15: Oscillatory flow in a parabolic bowl with friction. LTS-RKDG2 calculations vs. GTS-RKDG2 calculations across the x -direction centreline (a) baseline mesh 40×40 with $lev_{max} = 2$ and (b) baseline mesh 20×20 with $lev_{max} = 3$.

696



(a) (b)
Fig. 16: 2D breaking wave over dry floodplain with friction. Initial free-surface elevation condition, 2D domain and mesh configuration with refined portions; (a) $lev_{max} = 2$ and (b) $lev_{max} = 3$.

697

698 **6.5 2D breaking wave over dry floodplain with friction**

699 This test may be regarded as the 2D version of the test investigated in Subsection 6.3. It is
700 widely used as a 2D standard benchmark to assess the adequacy of computational flood
701 models for realistic applications [17]. The 2D domain is $[0; 75\text{m}] \times [0; 30\text{m}]$ that is assumed to
702 be enclosed by solid-walls and to initially hold a tranquil water body of 1.875m upstream of a
703 dam located at $x = 16\text{m}$. Downstream of the dam, the floodplain is dry with three topographic
704 hills (see Fig. 16) and is characterized by a roughness Manning coefficient of 0.0185. 2D-
705 LTS-RKDG2 and 2D-GTS-RKDG2 simulations are executed on a mesh of type *mesh-3LTSs*
706 and *mesh-4LTSs*, respectively, which are described in Table 8 and illustrated in Fig. 16. The
707 2D contour maps of the free-surface elevation produced by the RKDG2 models at $t = 6\text{s}$, 12s,
708 and 24s are presented in Fig. 17 (*mesh-3LTSs*) and Fig. 18 (*mesh-4LTSs*). On both meshes,
709 the LTS- and GTS-RKDG2 versions predicted nearly similar local of flow features (of shock,
710 smooth and wet/dry character). However, the contour patterns among the LTS-RKDG2 and
711 GTS-RKDG2 schemes correlate much better on *mesh-3LTSs* where the LTS-RKDG2
712 coordinate less LTSs (contrast Fig. 17 vs. Fig. 18). Whereas, on *mesh-4LTSs* the LTS-
713 RKDG2 predictions are more deviated and thus again indicate of a cumulative effect
714 associated with the depth of refinement levels.

715
716

Table 8: Mesh and runtime ratios after 24s for test-case 6.5

<i>Simulation case</i>	2D	
<i>Level of refinement</i>	2	3
<i>Baseline mesh</i>	40×20	20×10
<i>Domain</i>	$[0;75] \times [0;30]$	$[0;75] \times [0;30]$
<i>Runtime ratio (GTS/ LTS)</i>	0.5X	0.98X

717

718 In terms of runtime cost (Table 8) no runtime saving are here noted in the LTS-RKDG2
719 models performance, over the traditional GTS version. Possibly, such inefficiency is
720 associated with the relatively high number of fine-cells and the presence of very high
721 velocities. This suggests that the LTS-RKDG2 model would be able to speed-up simulation

722 times, in 2D, when the percentage of fine cells represents a very small portion of the 2D mesh
 723 and for low flow speed.

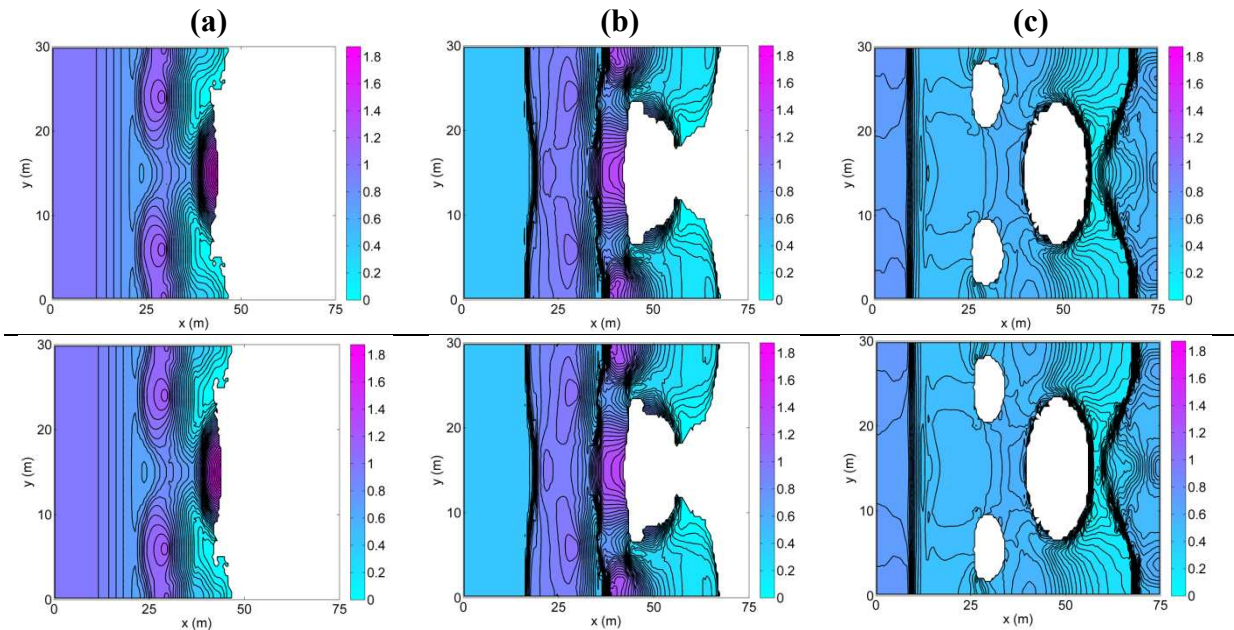


Fig. 17: 2D breaking wave over dry floodplain with friction. Contrasting the free-surface elevation contours obtained by the LTS-RKDG2 (lower panel) and the GTS-RKDG2 (upper panel) for $lev_{max} = 2$; (a) $t = 6s$, (b) $t = 12s$ and (c) $t = 24s$.

724

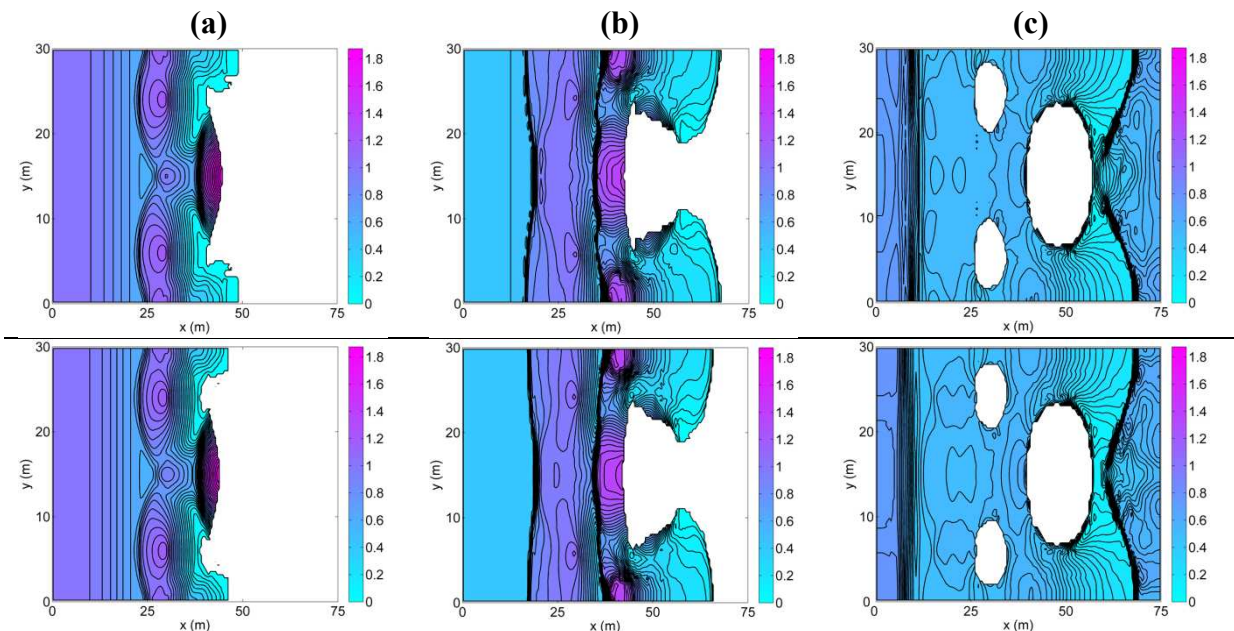


Fig. 18: 2D breaking wave over dry floodplain with friction. Contrasting the free-surface elevation contours obtained by the LTS-RKDG2 (lower panel) and the GTS-RKDG2 (upper panel) for $lev_{max} = 3$; (a) $t = 6s$, (b) $t = 12s$ and (c) $t = 24s$.

725

726 7. Conclusions

727 A LTS algorithm [24], which involves a small calculation stencil, has been integrated with a
728 robust RKDG2 shallow water model on structured non-uniform meshes (LTS-RKDG2). Most
729 advanced stabilizing features that enable the practical use of shallow water numerical models
730 – previously available within the traditional GTS-RKDG2 version, i.e. for controlling slope
731 coefficients, handling complex domain topography and wetting and drying [17] – were
732 retained within the LTS-RKDG2 design. However further considerations were given to
733 maintain the flux conservation (in time) across cells of different sizes, and to diminish the
734 adverse effects of the IFTD (Implicit Friction Term Discretisation). 1D and 2D versions of
735 the LTS-RKDG2 model were setup and ran on non-uniform meshes of type ‘*mesh-3LTSs*’
736 and ‘*mesh-4LTSs*’ that, respectively, comprised ‘3’ and ‘4’ levels of local spatial
737 discretization (e.g., $\{\Delta x, \Delta x/2, \Delta x/4\}$ and $\{\Delta x, \Delta x/2, \Delta x/4, \Delta x/8\}$ for the 1D meshes). On
738 these meshes, the LTS-RKDG2 model adapted correspondingly LTSs of $\{\Delta t, \Delta t/2, \Delta t/4\}$ and
739 $\{\Delta t, \Delta t/2, \Delta t/4, \Delta t/8\}$, whereas the GTS-RKDG2 model used the smallest GTS allowable.
740 Selected test cases were employed to verify the LTS-RKDG2 models’ implementation with
741 respect to the associated GTS-RKDG2 schemes considering realistic aspects of hydraulic
742 modelling.

743 In all tests, the LTS-RKDG2 schemes were able to generically produce very close
744 prediction as the GTS-RKDG2 despite the presence of water jumps, irregular topographies
745 and wetting and drying. A closer analysis of the results, however, suggest that the LTS-
746 RKDG2 model might lose its exponential convergence property for steady state simulations,
747 its overall second-order mesh-convergence for the case involving more depth in the spatio-
748 temporal refinement increasingly with the dimensionality of the formulation and the deepness
749 of refinement levels.

750
751

Table 9: Range of the relative runtime savings.

<i>Runtime ratio (GTS/GLS)</i>	<i>1D simulations</i>	<i>2D simulations</i>
<i>Mesh of type “mesh-3LTSs”</i>	1.3—2.0X	0.18—1.6X
<i>Mesh of type “mesh-4LTSs”</i>	1.36—2.5X	0.98—1.5X

752

753

754

755

756

757

758

759

760

761

762

In terms of runtime saving relative to the GTS-RKDG2 simulations, for the test cases investigated in this study (Table 9), the 1D LTS-RKDG2 formulation has speeded up efficiency by an average factor of 2; whereas, the 2D formulation relatively offered saving of around average factor of 1.6. The maximum efficiency speed up has been observed in the tests involving a relatively small proportion of fine cells (Subsection 6.1) and/or a low velocity flows (Subsection 6.2), and when more levels of spatio-temporal adaptation have been employed (*mesh-4LTSs*). For violent flows and/or cases where the mesh involves a significant portion of fine cells, LTS-RKDG2 models have been found to be much less effective. Most notably, its 2D formulation has provided very little saving for on meshes of type *mesh-4LTSs* and no saving at all for meshes of type *mesh-3LTSs*.

763

764

765

766

767

768

769

770

771

772

Based on the present findings, we essentially recommend the use of LTS-RKDG2 model on non-uniform meshes in which the refined portion constitutes a very small percentage of the global domain, namely in 2D simulations. Otherwise, the saving in runtime gained by the integration of the LTS algorithm would be eliminated by extra operational cost entailed at those cells that are smaller than the coarsest cells. Moreover, in the interest of accuracy, conservation and economy, it would be further beneficial to tailor a LTS-RKDG2 version with the least levels of LTSs. The improvement and/or extension of proposed LTS approach to higher than second-order RKDG formulation is hindered by the need of more comprehensive space-time interpolation formula and the need to cope with more inner stages within the RK mechanism.

773 **Acknowledgement**

774 The present work was partially developed within the framework of the Panta Rhei Research
775 Initiative of the International Association of Hydrological Sciences. This research is
776 supported by the UK Engineering and Physical Sciences Research Council (grants ID:
777 EP/F030177/1 and EP/K031023/1).

778 **References**

- 779 1. Guinot, V., ed. *Godunov-type schemes: an introduction for engineers*. 2003, Elsevier:
780 Amsterdam.
- 781 2. Toro, E.F., ed. *Shock-capturing methods for free-surface shallow flows*. 2001, John
782 Wiley & Sons, Ltd.
- 783 3. Toro, E.F. and García-Navarro, P., *Godunov-type methods for free-surface shallow*
784 *flows: A review*. Journal of Hydraulic Research, 2007. **45**(6): p. 736-751.
- 785 4. Delis, A.I. and Kampanis, N.A., *Numerical flood simulation by depth averaged free*
786 *surface flow models*, in *Environmental Systems, in Encyclopedia of Life Support*
787 *Systems (EOLSS)*, A. Sydow, Editor. 2009.
- 788 5. Gallegos, H.A., Schubert, J.E., and Sanders, B.F., *Two-dimensional, high-resolution*
789 *modeling of urban dam-break flooding: A case study of Baldwin Hills, California*.
790 *Advances in Water Resources*, 2009. **32**(8): p. 1323-1335.
- 791 6. Liang, Q., Du, G., Hall, J.W., and Borthwick, A.G.L., *Flood Inundation Modeling*
792 *with an Adaptive Quadtree Grid Shallow Water Equation Solver*. Journal of Hydraulic
793 Engineering, 2008. **134**(11): p. 1603-1610.
- 794 7. Lacasta, A., García-Navarro, P., Burguete, J., and Murillo, J., *Preprocess static*
795 *subdomain decomposition in practical cases of 2D unsteady hydraulic simulation*.
796 *Computers & Fluids*, 2013. **80**(0): p. 225-232.

- 797 8. Sanders, B.F., Schubert, J.E., and Detwiler, R.L., *ParBreZo: A parallel, unstructured*
798 *grid, Godunov-type, shallow-water code for high-resolution flood inundation*
799 *modeling at the regional scale*. *Advances in Water Resources*, 2010. **33**(12): p. 1456-
800 1467.
- 801 9. Brodtkorb, A.R., Sætra, M.L., and Altinakar, M., *Efficient shallow water simulations*
802 *on GPUs: Implementation, visualization, verification, and validation*. *Computers &*
803 *Fluids*, 2012. **55**(0): p. 1-12.
- 804 10. Smith, L.S. and Liang, Q., *Towards a generalised GPU/CPU shallow-flow modelling*
805 *tool*. *Computers & Fluids*, 2013. **88**(0): p. 334-343.
- 806 11. Eskilsson, C., El-Khamra, Y., Rideout, D., Allen, G., Chen, Q.J., and Tyagi, M., *A*
807 *Parallel High-Order Discontinuous Galerkin Shallow Water Model*, in
808 *Computational Science – ICCS 2009*, G. Allen, et al., Editors. 2009, Springer Berlin
809 Heidelberg. p. 63-72.
- 810 12. Courant, R., Friedrichs, K., and Lewy, H., *Über die partiellen Differenzgleichungen*
811 *der mathematischen Physik*. *Mathematische Annalen*, 1928. **100**(1): p. 32-74.
- 812 13. Zhou, T., Li, Y., and Shu, C.W., *Numerical comparison of WENO finite volume and*
813 *Runge–Kutta discontinuous Galerkin methods*. *Journal of Scientific Computing*, 2001.
814 **16**(2): p. 145-171.
- 815 14. Zhang, M. and Shu, C.W., *An analysis of and a comparison between the*
816 *discontinuous Galerkin and the spectral finite volume methods*. *Computers & Fluids*,
817 2003. **34**(4-5): p. 581-592.
- 818 15. Kesserwani, G. and Liang, Q., *Locally Limited and Fully Conserved RKDG2 Shallow*
819 *Water Solutions with Wetting and Drying*. *Journal of Scientific Computing*, 2012: p.
820 1-25.

- 821 16. Kesserwani, G. and Liang, Q., *A discontinuous Galerkin algorithm for the two-*
822 *dimensional shallow water equations*. Computer Methods in Applied Mechanics and
823 Engineering, 2010. **199**(49-52): p. 3356-3368.
- 824 17. Kesserwani, G. and Liang, Q., *Dynamically adaptive grid based discontinuous*
825 *Galerkin shallow water model*. Advances in Water Resources, 2012. **37**: p. 23-39.
- 826 18. Wirasaet, D., Tanaka, S., Kubatko, E.J., Westerink, J.J., and Dawson, C., *A*
827 *performance comparison of nodal discontinuous Galerkin methods on triangles and*
828 *quadrilaterals*. International Journal for Numerical Methods in Fluids, 2010. **64**(10-
829 12): p. 1336-1362.
- 830 19. Crossley, A.J. and Wright, N.G., *Time accurate local time stepping for the unsteady*
831 *shallow water equations*. International Journal for Numerical Methods in Fluids,
832 2005. **48**(7): p. 775-799.
- 833 20. Sanders, B.F., *Integration of a shallow water model with a local time step*. Journal of
834 Hydraulic Research, 2008. **46**(4): p. 466-475.
- 835 21. Constantinescu, E. and Sandu, A., *Multirate Timestepping Methods for Hyperbolic*
836 *Conservation Laws*. Journal of Scientific Computing, 2007. **33**(3): p. 239-278.
- 837 22. Seny, B., Lambrechts, J., Comblen, R., Legat, V., and Remacle, J.F., *Multirate time*
838 *stepping for accelerating explicit discontinuous Galerkin computations with*
839 *application to geophysical flows*. International Journal for Numerical Methods in
840 Fluids, 2013. **71**(1): p. 41-64.
- 841 23. Trahan, C.J. and Dawson, C., *Local time-stepping in Runge–Kutta discontinuous*
842 *Galerkin finite element methods applied to the shallow-water equations*. Computer
843 Methods in Applied Mechanics and Engineering, 2012. **217–220**(0): p. 139-152.
- 844 24. Krivodonova, L., *An efficient local time-stepping scheme for solution of nonlinear*
845 *conservation laws*. Journal of Computational Physics, 2010. **229**(22): p. 8537-8551.

- 846 25. Krivodonova, L., Xin, J., Remacle, J.F., Chevaugeon, N., and Flaherty, J.E., *Shock*
847 *detection and limiting with discontinuous Galerkin methods for hyperbolic*
848 *conservation laws*. Applied Numerical Mathematics, 2004. **48**(3-4): p. 323-338.
- 849 26. Xing, Y. and Shu, C.W., *A new approach of high order well-balanced finite volume*
850 *WENO schemes and discontinuous Galerkin methods for a class of hyperbolic*
851 *systems with source terms*. Communication in Computational Physics, 2006. **1**(1): p.
852 101-135.
- 853 27. Liang, Q. and Marche, F., *Numerical resolution of well-balanced shallow water*
854 *equations with complex source terms*. Advances in Water Resources, 2009. **32**(6): p.
855 873-884.
- 856 28. Audusse, E., Bouchut, F., Bristeau, M., Klein, R., and Perthame, B., *A fast and stable*
857 *well-balanced scheme with hydrostatic reconstruction for shallow water flows*. SIAM
858 Journal on Scientific Computing, 2004. **25**(6): p. 2050-2065.
- 859 29. Kesserwani, G., Liang, Q., Vazquez, J., and Mosé, R., *Well-balancing issues related*
860 *to the RKDG2 scheme for the shallow water equations*. International Journal for
861 Numerical Methods in Fluids, 2010. **62**(4): p. 428-448.
- 862 30. Brufau, P., Vázquez-Cendón, M.E., and García-Navarro, P., *A numerical model for*
863 *the flooding and drying of irregular domains*. International Journal for Numerical
864 Methods in Fluids, 2002. **39**(3): p. 247-275.
- 865 31. Bader, M., Bock, C., Schwaiger, J., and Scaba, B., *Dynamically adaptive simulations*
866 *with minimal memory requirement—solving the shallow water equation using*
867 *sierpinski curves*. SIAM Journal Scientific Computing, 2010. **32**(1): p. 212-228.
- 868 32. Cockburn, B. and Shu, C.-W., *The Runge-Kutta local projection P1-discontinuous*
869 *Galerkin method for scalar conservation laws*. RAIRO Modél Math Anal Numér
870 1991. **25**(3): p. 337–361.

- 871 33. Cockburn, B. and Shu, C.-W., *Runge-Kutta discontinuous Galerkin methods for*
872 *convection-dominated problems*. Journal of Scientific Computing, 2001. **16**(3): p.
873 173-261.
- 874 34. Shu, C.-W. and Osher, S., *Efficient implementation of essentially non-oscillatory*
875 *shock-capturing schemes*. Journal of Computational Physics, 1988. **77**(2): p. 439-471.
- 876 35. Kesserwani, G. and Liang, Q., *Locally Limited and Fully Conserved RKDG2 Shallow*
877 *Water Solutions with Wetting and Drying*. J. Sci. Comput., 2012. **50**(1): p. 120-144.
- 878 36. Burguete, J., Garcia-Navarro, P., Murillo, J., and Garcia-Palacin, I., *Analysis of the*
879 *Friction Term in the One-Dimensional Shallow-Water Model*. Journal of Hydraulic
880 Engineering, 2007. **133**(9): p. 1048-1063.
- 881 37. Murillo, J., García-Navarro, P., and Burguete, J., *Time step restrictions for well-*
882 *balanced shallow water solutions in non-zero velocity steady states*. International
883 Journal for Numerical Methods in Fluids, 2009. **60**(12): p. 1351-1377.
- 884 38. Meselhe, E.A., Sotiropoulos, F., and Holly Jr, F.M., *Numerical Simulation of*
885 *Transcritical Flow in Open Channels*. Journal of Hydraulic Engineering, 1997.
886 **123**(9): p. 774-783.
- 887 39. Kesserwani, G. and Liang, Q., *Influence of Total-Variation-Diminishing Slope*
888 *Limiting on Local Discontinuous Galerkin Solutions of the Shallow Water Equations*.
889 Journal of Hydraulic Engineering, 2012. **138**(2): p. 216-222.
- 890 40. Heniche, M., Secretan, Y., Boudreau, P., and Leclerc, M., *A two-dimensional finite*
891 *element drying-wetting shallow water model for rivers and estuaries*. Advances in
892 Water Resources, 2000. **23**(4): p. 359-372.
- 893 41. Hiver, J.M. *Adverse-slope and slope (bump)*. in *Concerted Action on Dam Break*
894 *Modelling: Objectives, Project Report, Test Cases, Meeting Proceedings*. 2000.

895 Université catholique de Louvain, Civ. Eng. Dept., Hydraulics Division, Louvain-la-
896 Neuve, Belgium.

897 42. Sampson, J., Easton, A., and Singh, M. *Moving Boundary Shallow Water Flow in*
898 *Circular Paraboloidal Basins*. in *EMAC 2003 Proceedings: 5th International*
899 *Congress on Industrial and Applied Mathematics*. 2003: University of Technology,
900 Sydney - Faculty of Science.

901

902